*Journal of Biomedical Materials Research Part A*

WILEY

Society For Biomaterials

RESEARCH ARTICLE OPEN ACCESS

# Bilayer Fiber-Reinforced Composite-Hydrogel Scaffolds With Bioactive Glass for Bone Tissue Regeneration

Mona Gibreel[1] | Roope Ohlsbom[2,3] | Leila Perea-Lowery[1] | Lippo Lassila[1] | Paula Puistola[4] | Karoliina Hopia[4] | Susanna Miettinen[2,3] | Anni Mörö[4] | Pekka K. Vallittu[1,5]

[1]Department of Biomaterials Science and Turku Clinical Biomaterials Center-TCBC, Institute of Dentistry, University of Turku, Turku, Finland | [2]Adult Stem Cell Group, Faculty of Medicine and Health Technology, Tampere University, Tampere, Finland | [3]Tays Research Services, Wellbeing Services County of Pirkanmaa, Tampere University Hospital, Tampere, Finland | [4]Eye Regeneration Group, Faculty of Medicine and Health Technology, Tampere University, Tampere, Finland | [5]The Wellbeing Services County of Southwest Finland, Turku, Finland

**Correspondence:** Mona Gibreel (mona.f.gibreel@utu.fi)

**Received:** 22 July 2025 | **Revised:** 7 January 2026 | **Accepted:** 13 January 2026

**Keywords:** 3D printing | bioactive glass | bone regeneration | composite | fiber | hydrogel

## ABSTRACT

Bone tissue regeneration for large defects presents a significant challenge, demanding scaffolds that combine robust mechanical support alongside a bioactive environment. Hydrogels represent a promising solution for bone regeneration due to their biocompatibility, tunable properties, and crosslinked three-dimensional (3D) networks mimicking the natural extracellular matrix (ECM). However, their mechanical properties remain suboptimal for restoring bone defects effectively. This study introduces a novel bilayer laminate scaffold, integrating a biostable fiber-reinforced composite (FRC) with a biodegradable, 3D-printed hyaluronic acid (HA)-based hydrogel. To enhance bioactivity, bioactive glass (BAG) was incorporated into the hydrogel layer. Comprehensive characterization confirmed the scaffold's chemical and morphological properties, as well as its controlled degradation, sustained ion release, and bioactivity. Additionally, the study revealed that the BAG-induced alkaline pH shift (up to 9.24) affected hydrazone crosslinking efficiency, resulting in reduced hydrogel stiffness ($86 \pm 8$ Pa versus $150 \pm 4$ Pa in control). The system showed excellent cytocompatibility, supporting high viability and proliferation of human bone marrow stem cells (BMSCs) embedded within the hydrogel component. The developed scaffolds promoted osteogenic differentiation, as evidenced by increased ALP activity and upregulated expression of osteogenic marker genes. Nevertheless, BAG incorporation did not enhance early osteogenic differentiation compared to control scaffolds. In conclusion, this bilayer scaffold offers a promising platform for bone tissue engineering (TE), providing some insights into the chemical interplay between inorganic fillers and hydrogel matrix for optimizing future scaffold designs.

## 1 | Introduction

Bone is a highly specialized, dynamic connective tissue comprising hydroxyapatite crystals embedded in a gel-like extracellular matrix (ECM) of proteins and polysaccharides [1]. Bone possesses the capacity for self-repair and regeneration through the coordinated activity of osteoblasts, osteoclasts, and osteocytes [2]. However, critical-sized defects arising from trauma or tumor resection exceed the bone's intrinsic repair capacity [3]. Although bone grafting remains the primary treatment for such defects, autografts require an additional surgical intervention and carry risks of donor-site morbidity [4]. Conversely, allografts and xenografts, while viable alternatives, introduce histocompatibility antigens that increase the rejection risk [5].

Hydrogels are three-dimensional (3D) networks of hydrophilic natural or synthetic polymers crosslinked to form insoluble polymer matrices. Natural polymers such as collagen, gelatin,

and hyaluronan exhibit excellent biocompatibility, minimal immunogenicity and cytotoxicity, and promote cell adhesion, proliferation, and new tissue formation [6]. Hydrogel scaffolds mimic the bone ECM and have the capacity to encapsulate bioactive particles or cells. Their porous network structure enables controlled release of entrapped agents or drugs, facilitates nutrient diffusion and cellular metabolic waste removal, and supports tissue integration due to their bioresorbable nature, thereby minimizing the need for surgical removal and reducing the risk of inflammatory responses [7].

Hyaluronic acid (HA), a natural unbranched polysaccharide, is widely used in tissue engineering (TE) applications [8]. HA is biocompatible, biodegradable, hydrophilic, supports cell signaling, wound healing, matrix organization, and exhibits anti-inflammatory properties. Nevertheless, its poor mechanical strength and rapid degradation limit its suitability for 3D bioprinting [9]. Therefore, HA is frequently chemically modified with functional groups to enhance the stability of HA-based bioinks. For instance, photo-crosslinkable HA bioinks were obtained through functionalization with methacrylate [10], while alternative functionalization of HA with hydrazide and aldehyde groups enables hydrazone crosslinking [8]. Type I Collagen, a primary bone ECM protein [1], is commonly employed in bioinks for cell encapsulation due to its low immunogenicity and cell-binding motifs that enhance proliferation, adhesion, and attachment [11]. The composition and cross-linking density of bioinks critically influence their properties and cellular responses. Accordingly, different bioink systems employ various materials and crosslinking mechanisms to recapitulate the characteristics of specific tissues [9].

Extrusion-based and stereolithographic 3D bioprinting represent advanced biofabrication techniques in regenerative medicine, enabling precise, layer-by-layer construction of complex scaffolds that mimic native tissue architecture [9, 12, 13]. During bioprinting, bioinks comprising biomaterials, cells, and optionally growth factors are extruded according to a computer-aided design model in a reproducible manner [12].

Despite their advantages, hydrogels alone exhibit insufficient mechanical properties for effective bone defects reconstruction. To address this limitation, different strategies have been employed to enhance their mechanical competence, including the incorporation of nano- or micro-sized inorganic ceramics, which not only reinforce the matrix and mimic the physicochemical composition of bone but also provide nucleation sites for biomineralization [13, 14]. Among such reinforcements, bioactive glass (BAG) is a synthetic, silica-based biomaterial with bacteriostatic, osteoconductive, and osteoinductive properties. Clinically approved compositions BAG such as 45S5 and S53P4, are well known for their ability to interact chemically with bone [15]. Furthermore, the incorporation of BAG into gelatin-alginate hydrogel has been shown to enhance the osteogenic differentiation of human bone marrow stem cells (BMSCs). An alternative approach involves combining synthetic and natural polymers to engineer biomaterials with tuned properties matching the tissue of interest [16, 17]. Additionally, synthetic fibers or fibrous mesh can be incorporated within the hydrogel matrix to improve the mechanical integrity [9]. Dubey et al. [18] developed a PCL fiber-reinforced gelatin methacryloyl (GelMA) hydrogel with amorphous magnesium phosphate for guided bone regeneration, resulting in enhanced stiffness and favorable cellular responses. More recently, the combination of different materials using different fabrication techniques, such as electrospinning and 3D printing, has emerged as an effective strategy to obtain biomimetic laminate scaffolds with improved performance. As an example, a bilayer scaffold designed for interface TE application was fabricated by adhering a 3D-printed GelMA hydrogel to an electrospun polycaprolactone (PCL)-collagen fiber layer [19].

Fiber-reinforced composite (FRC) materials have been explored as implants for load-bearing applications, such as dental implants [20, 21]. Väisänen et al. [22] developed semi-anatomic glass FRC implants for reconstructing large mandibular segmental defects. FRC has been contemplated as a patient-specific implant for cranioplasty, as they can be contoured to the resected bone anatomy [23–25]. FRC implants are durable and biostable, with mechanical strength and elasticity that closely match the physiological requirements of bone [26, 27], while demonstrating good cytocompatibility comparable to that of titanium [20, 28, 29]. In vivo studies [21, 28] confirmed new bone formation within the lamellar and porous structure of FRC-BAG implants.

This study introduced a new bilayer laminate scaffold designed to address the complex requirements of bone defects reconstruction. It integrates a 3D bioprinted HA-based hydrogel, incorporating BAG and human BMSCs, with a biostable FRC layer. The FRC layer was intended to provide the essential mechanical strength and maintain structural integrity, while the bioprinted hydrogel offered a customizable, bioactive environment for cellular regeneration. Human BMSCs were selected for their established osteoblastic differentiation potential in bone TE-based treatments [30]. While strategic inclusion of BAG aimed to promote osteoinduction, its effect on the hydrogel's physical properties and subsequent cellular response was also evaluated. FRC was fabricated and characterized first, followed by bioprinting of cell-free or cell-laden hydrogel mixed with BAG on top of FRC to obtain the final FRC-hydrogel laminate scaffolds. To the best of our knowledge, this is the first development of a bilayer scaffold, integrating 3D-bioprinted hydrazone-crosslinked HA-based hydrogel with FRC for bone TE. The study design is illustrated in Figure 1.

## 2 | Materials and Methods

### 2.1 | Preparation and Characterization of FRC

#### 2.1.1 | Preparation of FRC

To prepare FRC implants, one layer of silanized woven E-glass fiber fabric (Ahlstrom Glassfibre Oy, Kotka, Finland) was impregnated in a resin matrix composed of 70% (w/w) bisphenol A glycidylmethacrylate (BisGMA, Esschem Europe Ltd) and 30% (w/w) triethylene glycol dimethacrylate (TEGDMA, Sigma-Aldrich Co. LLC) with 0.7% (w/w) camphorquinone (CQ) and 0.7% (w/w) 2-(dimethylamino) ethyl methacrylate (DMAEMA, Sigma-Aldrich Co. LLC). After 24 h, the

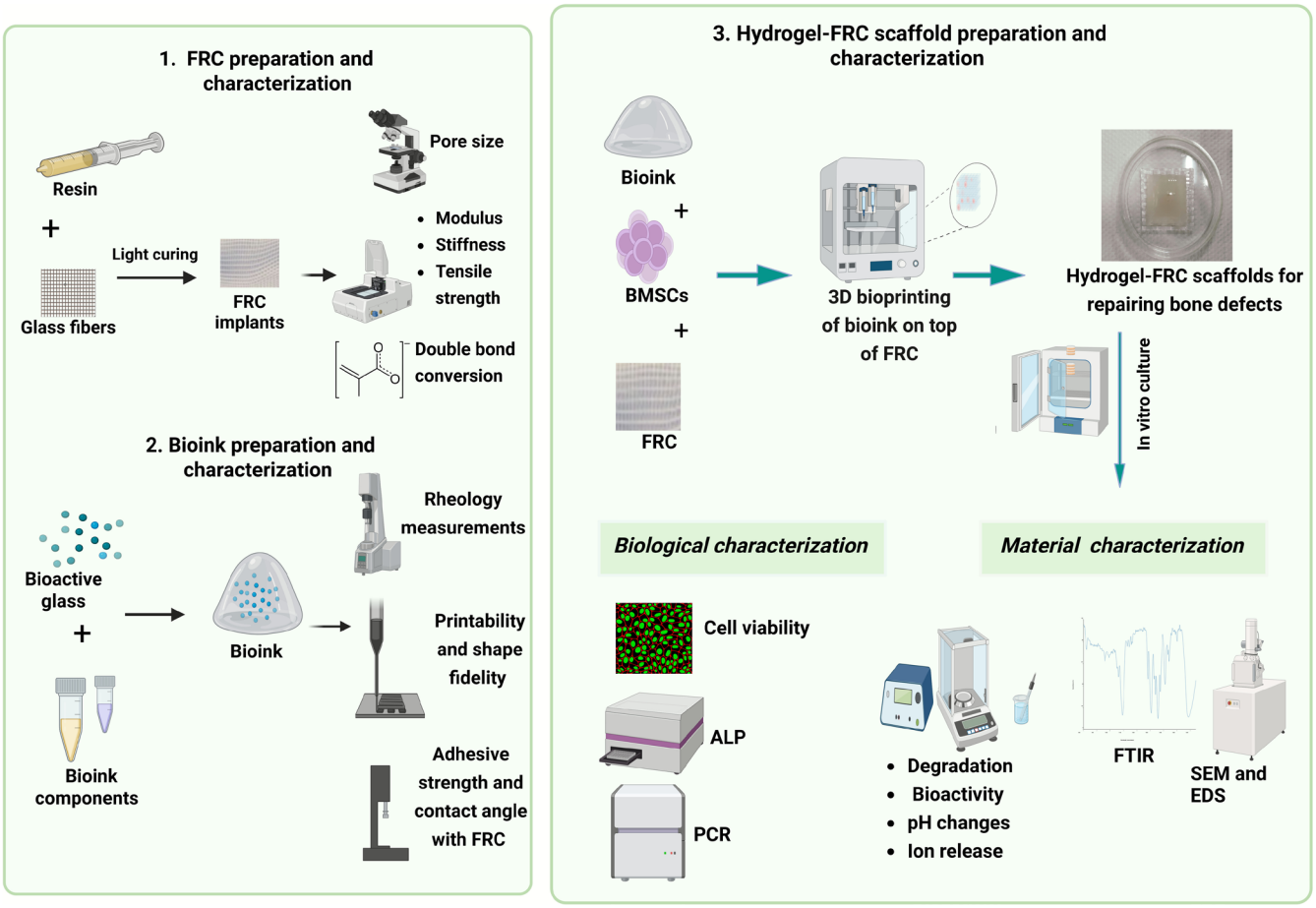


**FIGURE 1** | Schematic representation of workflow for preparation and characterization of HA-DA FRC and BAG-HA-DA FRC scaffolds.

impregnated fibers were cured in a light-curing oven with vacuum (Visio Beta Vario, Solventum (formerly 3 M ESPE), Seefeld, Germany) at 60°C for 15 min to eliminate the oxygen inhibition layer. Subsequently, the polymerization process was completed in another light-curing oven (Targis Power, Ivoclar Vivadent AG, Schaan, Lichtenstein) using a 467-nm wavelength beam for 25 min at 95°C. Sterilization of FRC was achieved by UV exposure for 20 min after immersion in 70% ethanol for 4 min. FRC implants used for biological tests were stored in 50 mL of distilled water for 48 h before bioprinting to allow the leaching of any residual unreacted monomers and free radicals, thereby minimizing potential cytotoxicity and enhancing the material's safety [31]. The cured FRC sheets were then cut into equal pieces (20 mm ± 2.0 mm × 20 mm ± 2.0 mm × 0.4 mm ± 0.1 mm and 15 mm ± 2.0 mm × 15 mm ± 2.0 mm × 0.4 mm ± 0.1 mm) and weighed using an analytical scale (XS105 DualRange, Mettler Toledo AG, Greifensee, Switzerland). Cured FRC implants ($n = 6$) were imaged with a stereomicroscope (Leica, Leica Microsystem GmbH, Wetzlar, Germany) to measure the pore size from three randomly selected pores in each.

### 2.1.2 | Degree of Conversion (DC %)

To measure the DC % for cured FRC, the absorbance intensities of the aliphatic C═C peak at 1673 $cm^{-1}$ and the reference peak at 1608 $cm^{-1}$ of both uncured resin and cured implants were measured with Fourier transform infrared (FTIR) spectroscopy (Spectrum One, Perkin-Elmer, Llantrisant, UK) in attenuated total reflection mode (ATR). Measurements were accumulations of 16 scans with a resolution of 4 $cm^{-1}$. The DC % was calculated using Equation (1), [32] where $C_{aliphatic}$ represented the absorption peak observed at 1637 $cm^{-1}$ and $C_{reference}$ represented the reference peak observed at 1607 $cm^{-1}$ in the cured FRC. Similarly, $U_{aliphatic}$ and $U_{reference}$ corresponded to the absorption peak at 1637 $cm^{-1}$ and the reference peak at 1607 $cm^{-1}$ in the uncured resin, respectively:

$$DC\ \% = \left(1 - \frac{C_{aliphatic}/C_{reference}}{U_{aliphatic}/U_{reference}}\right) \times 100 \quad (1)$$

### 2.1.3 | Mechanical Properties

The surface mechanical properties of FRC implants, including microhardness, elastic modulus, and stiffness, were evaluated by conducting an instrumented micro-indentation test ($n = 4$) using the Rtec SMT 5000 universal tribometer (Rtec Instruments, California, USA). The test was performed with a Berkovich diamond indenter at a constant peak load of 5 N applied perpendicular to the sample surface. Indentations were performed at two distinct points on each sample without interference. The loading and unloading times were set to 30 s. During each indentation cycle, the force-indentation

depth curves from each sample were plotted and analyzed using SMT software to calculate hardness ($H$) in GPa, elastic modulus ($E$) in GPa, and stiffness ($S$) in N/μm. $S$ was calculated from the slope of the unloading curve, while $H$ and $E$ were calculated according to Equations (2) and (3), where $F_m$ is the maximum force applied on the sample and $A_p$ is the cross-sectional area of the indenter tip at maximum depth. Values for each property were presented as mean ± standard deviation (SD).

$$H = \frac{F_m}{A_p} \tag{2}$$

$$E = f\left(S|A_p\right) \tag{3}$$

In addition, the tensile strength of FRC was evaluated using a tensile test. The test was conducted on cured FRC specimens ($n = 6$) (11 mm × 50 mm × 0.4 mm ± 0.1 mm) using a universal testing machine (LR30K plus, Lloyd Instruments, Fareham, UK) with a load cell of 5 kN at a speed of 5 mm min$^{-1}$ and at room temperature (23°C) under dry conditions with a gauge length of 20 mm. Results were analyzed with Nexygen software (Nexygen 4.0, Lloyd instruments Ltd., Fareham, UK).

## 2.2 | Preparation and Characterization of Bioink

### 2.2.1 | Preparation of Bioink

An HA-based hydrazone-crosslinked (HA-DA) bioink was prepared as described previously by Mörö et al. [8]. The grafting of dopamine (DA) onto HA and modifying it with carbodihydrazide (CDH) to obtain the HA-DA-CDH crosslinker was conducted following previously established procedures [8]. The 2nd crosslinker, HA-aldehyde (HA-ALD) was also synthesized as described before [12]. The synthesized HA-DA-CDH and HA-ALD (Figure S1) were freeze-dried and stored at −20°C until they were used. To prepare the HA-DA hydrogel, crosslinkers were first dissolved in sterile 1× PBS at a concentration of 14 mg mL$^{-1}$ and mixed with unmodified sodium hyaluronate (Novamatrix, Norway) (1% w/v) dissolved in 5× PBS with 0.4 M NaCl. Human collagen type I (OptiCol (3 mg/mL), Cell Guidance Systems Ltd., Cambridge, UK) neutralized to pH 7 with 0.1 M NaOH and 10× PBS (Carl Roth, Karlsruhe, Germany) was added, and mixing was done using a dual syringe system with a female–female Luer lock.

BAG-HA-DA bioink was prepared by mixing 10 mg/mL (equivalent to 1% w/v) of S53P4 BAG particles (BonaAlive Biomaterials, Turku, Finland) (particle size of < 45 μm) with the bioink components. The BAG particles underwent UV sterilization for 20 min before use.

### 2.2.2 | In Situ pH Measurement

The pH of HA-DA and BAG-HA-DA hydrogels was monitored. After mixing, 500 μL of each hydrogel was pipetted into an Eppendorf tube. The tubes were then placed inside an incubator at 37°C, and the pH of the hydrogels was measured at different time intervals over a period of 120 min using a calibrated pH meter (PHM220, Radiometer Analytical, Copenhagen, Denmark).

### 2.2.3 | Rheological Characterization

The rheological behavior of HA-DA and BAG-HA-DA hydrogels was evaluated using a 20 mm stainless-steel parallel plate geometry of a rheological rheometer (HAAKE RheoStress300, Thermo Fisher Scientific, Karlsruhe, Germany). Flow sweeps were performed at the printing temperature (20°C) with shear rates of 0.01–10 s$^{-1}$ to determine their injectability and shear-thinning properties. Before measurement, 400 μL of hydrogel was allowed to equilibrate for 120 s at the experimental temperature. The viscosity of the hydrogels was tested at different time intervals (25, 45, 60, and 75 min) at a fixed shear rate of 0.01 s$^{-1}$. Disc-shaped samples of the crosslinked hydrogels (1.0 mm thickness × 20 mm Ø) were used for oscillatory frequency sweeps ($\omega = 0.1$–10 Hz, $\gamma = 0.002$) at 37°C within the hydrogels' linear viscoelastic region (LVR) detected from amplitude sweep test ($\omega = 1$ Hz, $\gamma = 0.001$–10).

### 2.2.4 | 3D Bioprinting Setup and Shape Fidelity Test

The printability of the HA-DA and BAG-HA-DA bioinks was assessed using a 3D extrusion-based bioprinter (3D-Bioplotter Manufacturer Series by EnvisionTEC, Gladbeck, Germany). Following comprehensive mixing, the bioinks were transferred into 30 cc Nordson EFD syringe barrels (Ohio, United States) and a cartridge piston was inserted into the barrel. The bioinks were allowed to pre-crosslink at room temperature (RT) for 20–45 min before printing. For printing, 22 G needles (CellInk, Sweden, Gothenburg) with a length of 0.50 in. and an inner diameter of 0.413 mm were utilized. Printing was done at RT on 35-mm TC-treated petri dishes (Corning, NY, USA). Perfactory RP software (EnvisionTEC, Gladbeck, Germany) was used to build 3D models with a 330-μm layer thickness (slice) interval in STL format.

To assess shape fidelity, both bioinks were printed in rectilinear grid patterns of four layers, each with dimensions of 20 mm × 20 mm. The printed filaments were separated by 3.2 mm, and alternating layers were printed at a 0/90° pattern orientation with a thickness of 330 μm. Both bioinks were executed at a feed rate of 11–13 mm/s and a pressure of 0.6–0.8 bar.

The printed structures were imaged with a high-definition charged-coupled device (CCD) camera attached to the dispensing head mount. Images were obtained immediately after printing and after 7 days of immersion in 1× PBS at 37°C ± 0.5°C (2 mL/sample). ImageJ processing and analysis software (National Institutes of Health, Bethesda, MD, USA) was used to measure the width of the printed hydrogel filaments and the pore factor ($n = 6$). Three randomly selected pores and filaments from each printed sample were included in the image analysis. The pore factor (Pr) was calculated using Equation (4), [8] where $L$ is the perimeter of the pore and $A$ is the pore area.

$$\mathrm{Pr} = \frac{L^2}{16\,A} \tag{4}$$

## 2.3 | Contact Angle (CA) and Adhesive Strength of the Hydrogel to FRC

To study the surface wettability of FRC with HA-DA and BAG-HA-DA hydrogels, the CA of hydrogel on solid FRC laminates was measured with the sessile drop method [33] using an optical tensiometer (Theta, Biolin Scientific Oy, Espoo, Finland) at RT. Measurements were done immediately after a 4.3-μl hydrogel droplet was placed on the surface of the FRC scaffold ($n = 3$). For each droplet, 120 photos were captured in 10 s. The Young-Laplace equation was used to determine the CA surrounding the droplet.

A lap shear test was used to evaluate the adhesive strength of HA-DA and BAG-HA-DA hydrogels to FRC. Rectangular equal pieces of FRC (50 mm length × 13 mm width × 0.8 mm ± 0.2 mm thickness) were prepared. A 0.7-mm thick layer of hydrogel was uniformly applied to a 10 mm × 12 mm area on the surface of one FRC piece using a polyvinylsiloxane (Lab-Putty, Coltène, Altstätten, Switzerland) hollow mold. The mold was removed and another similar piece of FRC was placed on top of the hydrogel (Figure S2). The hydrogel was allowed to stabilize at 37°C in a humid environment for 3 h before testing. The free ends of FRC pieces were clamped with manual vise grips. The force response was recorded while keeping one sheet fixed and moving the other sheet at a speed of 1.0 mm $min^{-1}$ using a universal testing machine (LR30K plus, Lloyds Instruments, Hampshire, UK) with a load cell of 250 N. The values were expressed as mean ± SD. The adhesive strength (kPa) was obtained by dividing the maximum load by the adhesion area.

## 2.4 | Preparation of Hybrid FRC-Hydrogel Laminate Scaffolds

The cell-free HA-DA FRC and BAG-HA-DA FRC implants were prepared by 3D printing of the HA-DA and BAG-HA-DA hydrogels, respectively, on top of the polymerized FRC implants (20 mm ± 2.0 mm × 20 mm ± 2.0 mm × 0.4 mm ± 0.1 mm). First, cured FRC pieces were placed within 35-well plates, and hydrogel cubic-shaped scaffolds (15 mm × 15 mm) were printed on top of them in 6 layers (0/90° pattern orientation, 330-μm layer thickness). Both bioinks were executed at a feed rate of 11–13 mm/s and a pressure of 0.6–0.8 bar. The distance between the strands was set at 1.1 mm. The printed structures were allowed to stabilize at 37°C with 5% $CO_2$ in a humid environment for 60 min before adding the medium. The margins of FRC overextended for 5 mm beyond the hydrogel in an onlay configuration, which can be perforated to accommodate fixation screws when used in clinical settings [23].

## 2.5 | Characterization of Hybrid FRC-Hydrogel Laminate Scaffolds

### 2.5.1 | Fourier Transforms Infrared Spectroscopy (FT-IR)

FTIR was used for analyzing the absorption spectra of freeze-dried HA-DA FRC and BAG-HA-DA FRC scaffolds ($n = 2$). All IR spectra were recorded within the range 600–4000 $cm^{-1}$ with a resolution of $cm^{-1}$ and 16 accumulation scans in ATR mode. Spectral data analysis, baseline correction, and normalization were made using Perkin-Elmer Spectrum software.

### 2.5.2 | Scanning Electron Microscopy (SEM) and Energy-Dispersive X-Ray Analysis (EDX) of the Scaffolds

The surface morphology of freeze-dried HA-DA FRC and BAG-HA-DA FRC laminate scaffolds was examined using SEM (TM4000plus, Hitachi, Tokyo, Japan) operated at a 15 kV extension voltage in low vacuum mode and equipped with Energy-Dispersive X-ray (EDX) (AZtec, Oxford Instruments, Abingdon, UK) detector for quantitative analysis of the composition.

### 2.5.3 | In Vitro Degradation of FRC-Hydrogel Laminate Scaffolds in PBS

In vitro degradation profiles of the plain FRC mesh, HA-DA FRC, and BAG-HA-DA FRC scaffolds were evaluated by immersing the scaffolds ($n = 3$/group) in 10 mL of 1× PBS solution (pH 7.4) for up to 28 days at 37°C ± 0.5°C. The scaffolds were weighed using an analytical scale (XS105 DualRange, Metler Toledo AG, Greifensee, Switzerland) before and after soaking each scaffold in 10 mL of PBS buffer for 1, 3, 7, 14, 21, and 28 days, while the medium was refreshed at each time point. Day 1 was used to standardize the weight of scaffolds at other time points when evaluating degradation. The remaining weight and fluid uptake percentages were calculated using Equations (5) and (6), [8] respectively, where $W_m$ represented the weight of the scaffold at each time point, $W_1$ represented the weight of the scaffold on day 1, and $W_0$ represented the weight of the dry scaffold on day 0 before soaking. The scaffolds were visually inspected for hydrogel detachment from the FRC at each time point.

$$\text{Remaining weight}\,\% = \frac{W_m}{W_1} \times 100 \tag{5}$$

$$\text{Fluid uptake}\,\% = \frac{W_m - W_0}{W_0} \times 100 \tag{6}$$

### 2.5.4 | pH Changes and Ion Release in PBS

Changes in pH were measured with an electrode (PHM220, Radiometer Analytical, Copenhagen, Denmark) at days 1, 3, 7, 14, 21, and 28. Inductively Coupled Plasma-Optical Emission Spectroscopy (ICP-OES, Perkin-Elmer Optima 5300DV, Waltham, MA, USA) was employed to quantify the concentrations of phosphorus (P) ($\lambda = 213.617$ nm), calcium (Ca) ($\lambda = 317.933$ nm), silica (Si) ($\lambda = 212.412$ nm), and sodium (Na) ($\lambda = 589.592$ nm) ions in the solution after samples immersion for 1, 3, 7, and 14 days. At the desired time point, 1 mL of the collected solution was diluted in ultrapure water (1:10) and acidified with concentrated nitric acid ($HNO_3$) for the analysis. The results were displayed as mean ± SD.

#### 2.5.5 | Bioactivity and Ion Release Ability of FRC-Hydrogel Scaffolds in SBF

The bioactivity of HA-DA FRC and BAG-HA-DA FRC scaffolds ($n = 3$) was investigated after 14 days of immersion in simulated body fluid (SBF) (pH 7.4) prepared as per the protocol established by Kokubo et al. [34]. SBF wasn't refreshed to study the precipitation of hydroxyapatite-like layers. Scaffolds were then removed and washed with distilled water before freeze-drying. The formation of hydroxyapatite crystals on the surface of the scaffolds was examined using SEM equipped with EDX. FT-IR was used for analyzing the absorption spectra of the scaffolds after immersion in SBF. In addition, the concentration of Ca ions in the solution was also measured over time using an ion-specific electrode (Orion Electrode, Orion Research Inc., Boston, MA, USA) connected to an ion analyzer by mixing each 6 mL of SBF with 0.1 mL of Ionic Strength Adjustor Buffer (ISA) solution (Orion 932,011 ISE Ionic Strength Adjustors, Thermo Fisher Scientific, Waltham, MA, USA) and analyzing the mixture. Degradation of the scaffolds and pH changes measurements were also evaluated after 1, 3, 7, 14, 21, and 28 days.

### 2.6 | Cytocompatibility and Osteogenic Activity of FRC-Hydrogel Scaffolds

#### 2.6.1 | Cell Culture and Bioprinting

Human BMSCs were isolated from a 90-year-old male donor undergoing an elective surgical procedure at Tampere University Hospital. The isolation was done as previously described [35] with written informed consent from the donor and under the approval of the Ethics Committee of Pirkanmaa Hospital District (R15174). The mesenchymal origin of the BMSCs was verified by the analysis of their osteogenic and adipogenic differentiation capacity and flow cytometric characterization of their cell surface markers (Table S1 and Figure S3). BMSCs were expanded in basic medium (BM) made up of Minimum Essential Medium α (MEM α, Thermo Fisher Scientific) supplemented with 1% penicillin/streptomycin (Lonza, Basel, Switzerland), and 5% human serum (Serana Europe GmbH, Pessin, Germany) at 37°C ± 0.5°C with 5% $CO_2$. The BMSCs were cultured and passaged in T175 flasks (Nunc EasYFlask, Thermo Fisher Scientific) until they reached 80%–100% confluency at passage 3.

The cells were detached using *TrypLE Select* (Gibco 12563-011; Thermo Fisher Scientific) and mixed with different bioinks at a cell density of $2.5 \times 10^6$ cells/mL using a luer-lock and two syringes. After loading the bioinks into the printing cartridges, they were first allowed to pre-crosslink at room temperature with visual inspection before printing, as mentioned earlier. Cubic structures of 10 mm × 10 mm with five layers (0.330 mm layer thickness) were printed on top of 15 mm ± 1.0 mm × 15 mm ± 1.0 mm × 0.4 mm ± 0.1 mm FRC meshes in separate 35-well plates. The strand distance was set at 1.1 mm. The printed constructions were incubated at 37°C and 5% $CO_2$ for 60 min before adding BM and incubation for 24 h before replacing it with osteogenic medium (OM) composed of BM supplemented with 10 mM ß-glycerophosphate, 250 μM L-ascorbic acid-2-phosphate (Sigma Aldrich, Germany), and 5 nM dexamethasone (Sigma-Aldrich, Germany). Medium change was carried out twice a week. The printing setup used for bioprinting of the 3D structures was the same as described earlier in Section 2.2.4.

#### 2.6.2 | Cell Viability

The viability of cells printed within the hydrogel component of the scaffolds was evaluated on days 1, 7, and 14 after bioprinting using LIVE/DEAD Viability/Cytotoxicity Kit for mammalian cells (Invitrogen, Thermo Fisher Scientific) and PrestoBlue assay (Thermo Fisher Scientific), respectively. For the LIVE/DEAD assay, cells were double-stained with calcein acetoxymethyl (Calcein AM, 667 nM) and ethidium homodimer-1 (EthD-1, 333 nM) according to the manufacturer protocol. After incubation for 35–40 min at 37°C ± 0.5°C, the samples were washed with PBS and imaged using a fluorescence microscope (Leica DMi8, Leica Microsystem GmbH, Wetzlar, Germany). The PrestoBlue assay was performed to evaluate the metabolic activity and viability of cells in line with the manufacturer instructions. The samples were incubated for one hour in BM (day 1) or OM (day 7 and day 14) containing 10% (V/V) PrestoBlue at 37°C ± 0.5°C in the same culture well-plate. After that, the absorbance of three replicates ($n = 3$) at 570 nm was quantified using a microplate reader (VICTOR Nivo Multimode Plate Reader, Perkin Elmer, Llantrisant, UK). The analysis was conducted on a sample size of three cell-laden scaffolds per group.

#### 2.6.3 | Cell Proliferation and Alkaline Phosphatase (ALP) Activity

The relative DNA amount in the HA-DA FRC and BAG-HA-DA FRC scaffolds was measured after 1, 7, and 14 days from culture using a CyQUANT Cell Proliferation Assay kit (Invitrogen, Thermo Fisher Scientific) according to the manufacturer's instructions. Scaffolds ($n = 3$/group) were collected at each time point and frozen at −80°C in a lysate solution of 0.1% Triton X-100 (Sigma-Aldrich). A proper amount of CyQUANT GR dye was mixed with Cell-lysis buffer and milliQ-WATER to prepare the working solution. After two freeze–thaw cycles, 20 μL aliquots of each lysate were pipetted into a 96-well plate and each was mixed with 180 μL of CyQUANT GR working solution. Fluorescence measurements were conducted using a microplate reader (VICTOR Nivo Multimode Plate Reader, Perkin-Elmer, Llantrisant, UK) at 480/520 nm.

The ALP activity was quantified after 7 and 14 days of scaffolds culture using the same Triton-X 100 cell lysates as cell proliferation using a commercial kit (Sigma-Aldrich). In brief, 20 μL of lysate were pipetted into a MicroAmp Optical 96-well plate (Applied Biosystems, Life Technologies) and mixed with 90 μL working solution containing 1:1 stock substrate solution (*p*-nitrophenol phosphate) (Sigma-Aldrich) and 1.5 M alkaline buffer solution (2-amino-2-methyl propanol) (Sigma-Aldrich). The reaction was stopped after 15 min incubation at 37°C by adding 50 μL 1 M NaOH (Sigma-Aldrich) per well. A microplate reader was used to measure fluorescence absorbances at a wavelength of 405 nm. Finally, the ALP activity was normalized to the DNA content in each scaffold.

#### 2.6.4 | Gene Expression Analysis

Relative expression levels of osteogenic marker genes were studied with quantitative real-time polymerase chain reaction (qRT-PCR). Studied genes included runt-related transcription factor 2 (RUNX2), alkaline phosphatase (ALPL), distal-less homeobox 5 (DLX5), and osteopontin (SP7). Glyceraldehyde 3-phosphate dehydrogenase (GAPDH) was used as a reference gene to normalize the gene expression data. The samples ($n = 4$/group) were collected on days 7 and 14 and frozen in TRIzol reagent (Thermo Fisher Scientifc) at −80°C until RNA extraction. The total RNA was extracted from the scaffold structures using TRIzol reagent, following manufacturer's instructions. The sample RNA was further purified with Nucleospin kit (Macherey-Nagel GmbH & Co., KG, Düren, Germany). The RNA concentration and quality were measured with a spectrophotometer (Nanodrop ND-1000, Nanodrop Technologies, Wilmington, DE, USA). The isolated RNA was then reverse transcribed to cDNA with the High-Capacity cDNA Reverse Transcriptase Kit (Thermo Fisher Scientific). Finally, qRT-PCR was performed with the QuantStudio 12 K Flex Real-Time PCR System (Applied Biosystems) using the TaqMan Fast Advanced Master Mix (Thermo Fisher Scientific) and TaqMan Gene Expression Assays (Thermo Fisher Scientific) according to the manufacturer's instructions. The following assays were used: RUNX2 (Hs01047973_m1), ALPL (Hs01029144_m1), DLX5 (Hs01573641_mH), SP7 (Hs01866874_s1), and GAPDH (Hs02786624_g1). Relative quantification of gene expression was performed using the $2^{-\Delta\Delta Ct}$ method [36].

### 2.7 | Statistical Analysis

All quantitative results were expressed as mean values ± SD. Data were analyzed for statistical significance between groups using SPSS (IPM SPSS Statistics, v27.0, IBM Corp, Armonk, NY, USA) and (R, v4.4.0, R Foundation for Statistical Computing, Vienna, Austria) using Kruskal-Wallis and Dunn's post hoc test with the Holm correction and Mann–Whitney $U$ test at the $p \leq 0.05$ significance level.

## 3 | Results and Discussion

This study introduced a new hybrid laminate scaffold designed for reconstructing bone by combining a biostable FRC with a biodegradable, 3D-printed HA-based hydrogel incorporating BAG. The scaffold design was intended to synergistically combine the mechanical strength of the FRC with the osteoinductive potential of BAG incorporated into the hydrogel component. Additionally, BMCs were mixed with the hydrogel component of the scaffold for 3D bioprinting of cell-laden laminate scaffolds.

The biocompatibility of FRC has been previously confirmed through both in vitro and preclinical studies [23, 25, 28]. Osteoblast cell culture models did not demonstrate any adverse reactions to FRC, while enhanced osteogenic differentiation was reported on BAG-coated FRC compared with titanium [28]. Moreover, FRC implants do not produce artifacts in diagnostic imaging modalities such as X-rays, computed tomography (CT), or magnetic resonance imaging (MRI) and do not interfere with radiotherapy [24]. Accordingly, FRC materials represent a promising platform for designing scaffolds that combine favorable mechanical performance with biological compatibility.

### 3.1 | Structural and Mechanical Characterization of FRC

The characterization of FRC revealed its suitability as a foundational layer for bone regeneration scaffolds. The FRC demonstrated a high DC of 69% ± 3.0%, indicating effective polymerization of the resin matrix. Morphologically, the prepared FRC exhibited a mesh-like porosity with pore dimensions of 0.9 mm ± 0.2 mm × 0.6 mm ± 0.2 mm in the $x$ and $y$ directions, respectively (Figure 2A), with an average weight of 135.2 ± 13 mg.

The assessment of the mechanical properties of FRC at the micro-scale level with microindentation test revealed an elastic modulus of 4.9 ± 0.8 GPa, a stiffness of 0.8 ± 0.1 N/μm, and a surface hardness of 33.4 ± 8.9 GPa (Figure 2B). These values suggest that FRC exhibits moderate stiffness combined with localized flexibility. It is worth mentioning that the physical and mechanical properties of FRC can be customized based on fiber length, direction, and volume fraction. FRC with a high E-glass fiber content (up to ca. 65 vol%) can exhibit high flexural strength up to 1250 MPa, surpassing the compressive strength range of cortical bone (100–230 MPa) [24]. Further macro-scale evaluation with tensile testing revealed a tensile strength of 124.6 ± 26.2 MPa and an elastic modulus of 4.4 ± 0.7 GPa (Figure 2C,D). For comparison, the tensile strength of human compact (cortical) bone has been reported to range approximately from 66 to 150 MPa, depending on anatomical site and testing conditions [37].

### 3.2 | Effect of BAG on pH of the Hydrogel

The in situ pH measurements revealed that HA-DA hydrogel displayed a stable, near-neutral pH (6.46) immediately after mixing, which remained almost constant throughout the measurement period (Figure S4). In contrast, BAG incorporation induced a rapid and substantial alkaline shift within the gel matrix. The BAG-HA-DA hydrogel exhibited an initial pH of 8.52 immediately after mixing, which increased to 9.24 after 120 min. This rapid increase in alkalinity is a direct consequence of the dissolution mechanism of S53P4 glass, which undergoes a rapid ion exchange process where alkaline cations ($Na^+$ and $Ca^{2+}$) are released into the surrounding aqueous environment, consuming $H^+$ ions and dramatically increasing local pH [38]. This observation demonstrates that BAG particles can actively modulate the hydrogel microenvironment instead of functioning as passive fillers.

### 3.3 | Rheological Characterization of the Bioink: Shear-Thinning Behavior and BAG-Induced Viscosity Modulation

Rheological characterization of HA-DA and BAG-HA-DA hydrogels revealed a shear-thinning behavior in both formulations, with viscosity decreasing as the shear rate increased

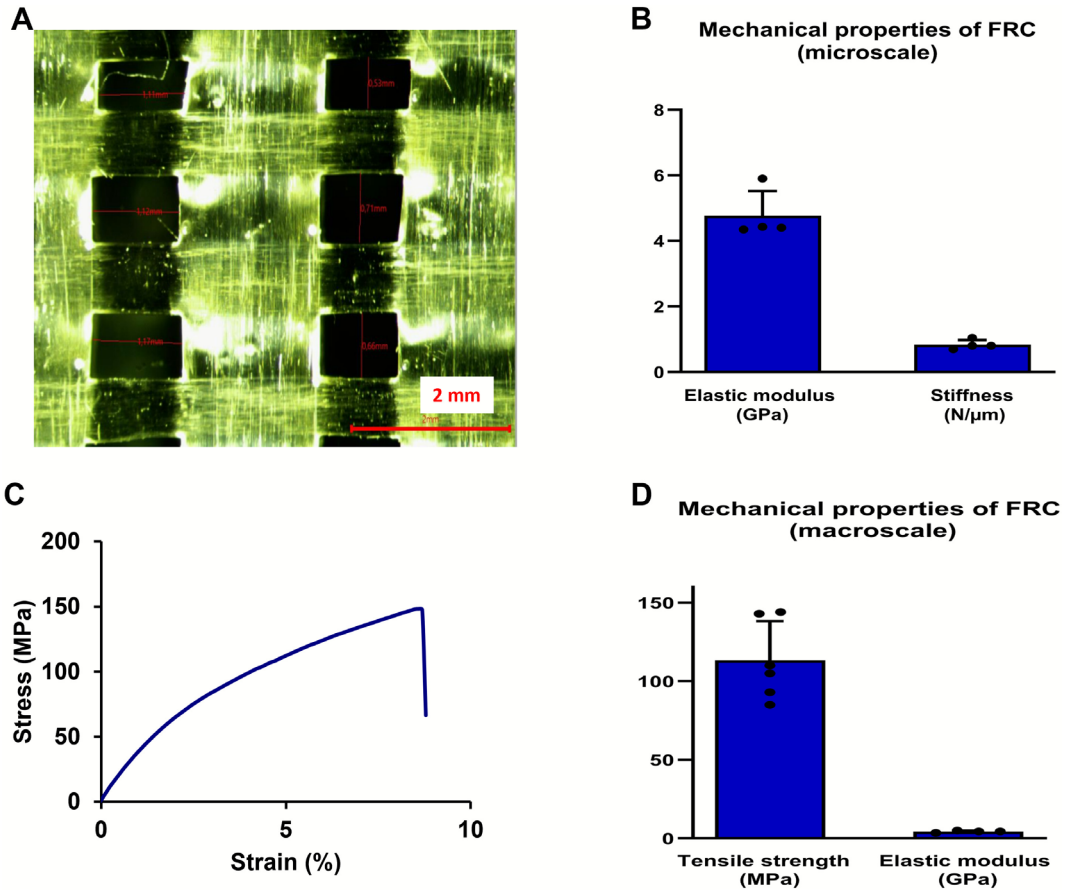


**FIGURE 2** | Characterization of FRC mesh. (A) Stereomicroscopic image of cured FRC mesh showing pore dimensions ($n = 6$). (B) Microscale mechanical properties of FRC ($n = 4$). (C) Stress–strain curve from tensile strength test of FRC. (D) Macroscale mechanical properties of FRC ($n = 6$). The data of (B, D) are expressed as the means ± SD.

(Figure 3A). This characteristic is essential for ensuring smooth extrusion through the bioprinter nozzle, facilitating precise fabrication of complex 3D structures with high shape fidelity.

A more detailed analysis of the hydrogels' rheological properties revealed critical interactions caused by BAG incorporation. Upon mixing, the crosslinking reaction was initiated in both hydrogels; however, differences in their kinetic profiles emerged over time. The BAG-HA-DA hydrogel consistently displayed lower viscosity at different time points compared to the plain HA-DA hydrogel. After 75 min of mixing, the viscosity of the BAG-HA-DA hydrogel reached 2442 ± 957 Pa.s, approximately half that of HA-DA (5209 ± 684 Pa.s) (Figure 3B), suggesting delayed or impeded crosslinking in the presence of BAG.

This observation was further corroborated by frequency sweep analysis. While both fully crosslinked hydrogels exhibited a viscoelastic solid behavior, with storage modulus (G′) exceeding loss modulus (G″), HA-DA hydrogel showed a significantly higher G′ (150 ± 4 Pa at 1 HZ) compared to that of BAG-HA-DA (86 ± 8 Pa; $p = 0.05$) (Figure 3C,D), demonstrating that adding BAG decreased the hydrogel stiffness. This finding contrasts with previous studies [13, 38], where BAG increased the stiffness and enhanced the viscoelastic characteristics of ionically-crosslinked systems such as gellan gum or gelatin-alginate hydrogels, highlighting the context-dependence of BAG–polymer interactions.

This 43% reduction in stiffness correlates directly with the rapid alkaline shift in hydrogel pH reported in Section 3.2 (pH > 8.5, peaking at 9.24) upon BAG addition. The highly alkaline microenvironment might have impaired protonation of reactive groups necessary for hydrazone bond formation between aldehyde and hydrazide functional groups [39], resulting in a softer hydrogel network with lower crosslinking density [40]. This interaction implies that BAG incorporation in this HA-DA hydrogel system can actively modulate the polymerization kinetics and final mechanical properties.

### 3.4 | Printability and Shape Fidelity of the Bioink

Examination of the printed grid structures (Figure 3E) revealed that both HA-DA and BAG-HA-DA hydrogels were able to form 3D structures with good shape fidelity, uniform filament width, and minimal variations in pore factor. The four-layer constructs yielded a stable 3D architecture without collapse, with preserved grid structure integrity and without major pattern defects. Both hydrogels had Pr values > 0.85 (0.87 ± 0.02 and 0.86 ± 0.03 for HA-DA and BAG-HA-DA, respectively) (Figure 3F). Pr influences cell growth, mechanical

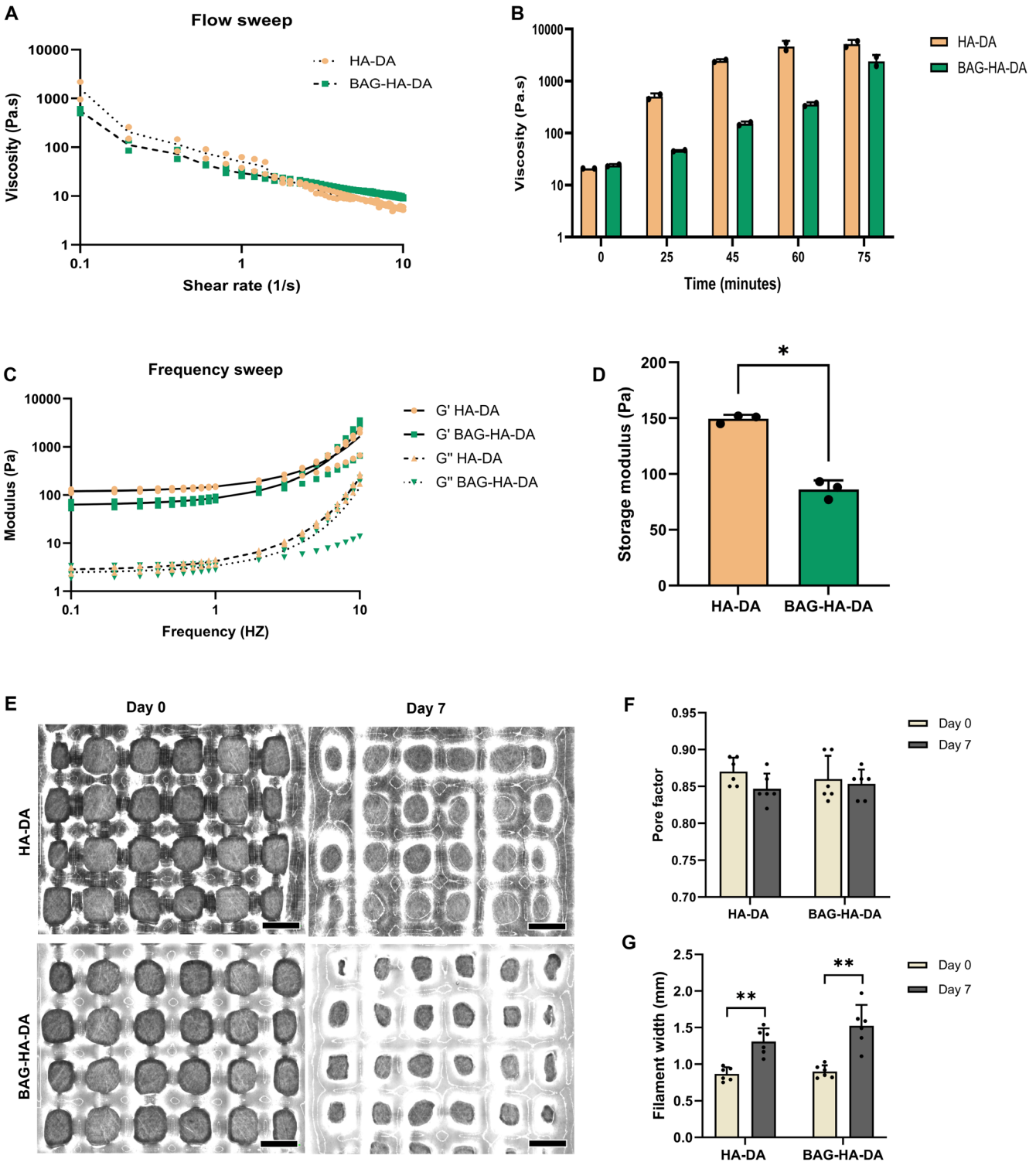


**FIGURE 3** | Rheological characterization and shape fidelity of HA-DA (control) and BAG-HA-DA (10 mg/mL, 1% w/v) hydrogels. (A) Flow sweep showing viscosities as a function of shear rate (0.01–10 $s^{-1}$) at 20°C ($n = 2$). (B) Time-dependent viscosity changes at fixed shear rate (0.01 $s^{-1}$) ($n = 2$). (C) Frequency sweep plots showing storage modulus ($G'$) and loss modulus ($G''$) of fully crosslinked hydrogels within the linear viscoelastic region at 37°C (frequency range: 0.1–10 Hz) ($n = 3$). (D) Quantitative comparison of mean storage modulus values of HA-DA and BAG-HA-DA hydrogels at 1 Hz ($n = 3$). (E) Representative optical images of 3D-printed four-layer grid structures (20 × 20 mm) of HA-DA and BAG-HA-DA hydrogels; scale bar = 2 mm. (F) Pore factor (Pr) analysis of printed grids of HA-DA and BAG-HA-DA hydrogels immediately after printing and following 7-day immersion in PBS at 37°C ($n = 6$). (G) Filament width of printed grids of HA-DA and BAG-HA-DA hydrogels immediately after printing and following 7-day immersion in PBS at 37°C ($n = 6$). *$p \leq 0.05$, **$p \leq 0.001$. The data of (A, B, C, D, F, G) are expressed as mean ± SD.

properties, and scaffold degradation rates; larger pores enhance nutrient diffusion and cell infiltration, promoting better cell growth, though they can affect the degradation rate and overall scaffold performance [41]. Filament width was 0.86 ± 0.1 mm for HA-DA and 0.90 ± 0.1 mm for BAG-HA-DA hydrogels (Figure 3G). Despite delayed crosslinking, the printability or shape fidelity of the BAG-HA-DA hydrogel was not compromised. After 7 days of incubation in PBS, the printed lattice structures maintained a visible grid structure and open pores (Figure 3E), with statistically similar Pr values for both hydrogels (0.84 ± 0.02 for HA-DA and 0.85 ± 0.02 for BAG-HA-DA; $p = 0.350$). However, filament width increased significantly (1.3 ± 0.2 mm and 1.5 ± 0.3 mm for HA-DA and BAG-HA-DA, respectively; $p < 0.001$) due to fluid absorption and swelling.

### 3.5 | Wettability and Adhesion of Hydrogel to FRC Driven by Dopamine and Mechanical Interlocking

Surface wettability can be determined by measuring the CA, which reflects the angle formed by the tangent line to the liquid droplet at the three-phase boundary and the horizontal surface of the solid interface [33]. This angle is defined by the balance between the cohesive forces of identical molecules (within the liquid) and the adhesive forces of different molecules (between the liquid and the solid surface) [42]. It reflects surface tension and the potential for capillary forces to influence the interaction of fluids on the scaffold surface [33]. The investigation of surface wettability and adhesive strength between FRC and HA-DA or BAG-HA-DA hydrogels revealed a strong interfacial bonding. CA readings were 66.43° ± 2.5 for the BAG-HA-DA and 62.24° ± 1.0 for HA-DA hydrogels ($p = 0.079$), showing no statistically significant difference and demonstrating good surface wettability and adhesion potential (Figure S5).

The mean adhesion strength values of HA-DA and BAG-HA-DA hydrogels to FRC, quantified with lap shear testing were 6.6 ± 2.3 and 15 ± 7.1 kPa, respectively. Although this difference was not statistically significant ($p = 0.121$), BAG-HA-DA hydrogel tended to exhibit higher adhesion to FRC, likely due to its lower viscosity and prolonged crosslinking time as discussed earlier in Section 3.3, allowing greater penetration into pores and surface microirregularities of the mesh.

The primary adherence of the HA hydrogel to the FRC was due to the DA grafted to the HA-DA-CDH crosslinker. DA, a catecholamine, is a key component in marine mussel adhesives, with high underwater or wet adhesiveness. It spontaneously polymerizes to form polydopamine, which adheres to many organic and inorganic surfaces through irreversible covalent and reversible non-covalent bonds such as strong hydrogen bonds via their dihydroxy functionality [43]. Furthermore, its benzene ring can interact with other aromatic rings through π–π interactions, or with positively charged ions through cation–π interactions [44]. Various synthetic polymers used in biomedical applications have been functionalized with catechols to provide diverse adhesive, sealant, coating, and anchoring properties [43, 44]. Furthermore, mechanical interlocking of the hydrogel within the FRC's surface microscopic roughness and mesh pores might have further enhanced interface adhesion and resistance to detachment.

### 3.6 | FTIR Analysis of Chemical Composition

FTIR spectroscopy identified the chemical structures of scaffold components and their interactions. Spectra of HA-DA FRC, BAG-HA-DA FRC, S53P4 BAG, and plain FRC are presented in Figure 4. In HA-DA FRC scaffolds, the spectrum displayed characteristic peaks consistent with its composition. A broad peak at 3100–3500 $cm^{-1}$ reflected the stretching vibrations of hydroxyl (O–H) and amide (N–H) groups in the HA-DA complex. The alkyl (C–H) stretching peak appeared at 2963 $cm^{-1}$, while the peaks at ~1610 and 1638 $cm^{-1}$ were assigned to hydrazone (C═N) stretching [39]. Also, amide II and III peaks were observed at nearly 1561 and 1260 $cm^{-1}$, respectively [8, 39]. A peak around 1032 $cm^{-1}$ was identified as the asymmetric stretching of C–O–C hemiacetal saccharide units in the hyaluronan backbone, while peaks for the asymmetric stretching vibrations of carboxylate ($–COO^-$) appeared at 1375–1405 $cm^{-1}$ [8].

S53P4 BAG powder exhibited characteristic peaks at nearly 915 $cm^{-1}$ attributed to the stretching vibrations of Si–O bands in $SiO_4^{4-}$ groups and around 1000 $cm^{-1}$ for Si–O–Si asymmetric stretching [38]. The symmetric bending vibration of O–Si–O was identified at ~730 $cm^{-1}$ [38]. A peak related to $CO_3^{2-}$ stretching vibration was also evident at 1460 $cm^{-1}$ [45].

BAG-HA-DA FRC scaffolds showed evidence of BAG integration. Additional, small shoulders at 960 and 894 $cm^{-1}$ were attributed to Si–O–Si stretching [46]. The peak at 1032 $cm^{-1}$ shifted to a lower wavelength (1021 $cm^{-1}$), suggesting changes in the local C–O bond environment. Furthermore, the peaks at 797, 1260, and 2963 $cm^{-1}$ showed a noticeable decrease in intensity, suggesting an altered chemical environment or a decrease in concentrations after BAG addition, possibly due to interactions with the released ions.

Plain cured FRC showed a broad peak at nearly 3300 $cm^{-1}$, corresponding to O–H stretching vibrations from BISGMA. Also, a peak for carbonyl (C═O) stretching vibrations from the polymer backbone was observed at nearly 1720 $cm^{-1}$. Peaks at 1607 and 1637 $cm^{-1}$ were characteristic of aromatic $C{=}C_{Ph}$ and methacrylic $C{=}C_{meth}$ double bond stretching, respectively. Aliphatic C–H peaks were observed at 1450–1500 $cm^{-1}$, while a peak for C–O stretching appeared at 1250 $cm^{-1}$, reflecting the presence of glycidyl and methacrylate functionalities [47, 48].

### 3.7 | Morphological and Elemental Analyses With SEM and EDS

The general view of laminate FRC-hydrogel scaffolds distinctly illustrated the successful formation of bilayer architecture (Figure S6A). Detailed SEM micrographs of the freeze-dried HA-DA FRC hydrogel surface (Figure S6B) revealed a relatively smooth morphology. EDX showed the presence of carbon (C),

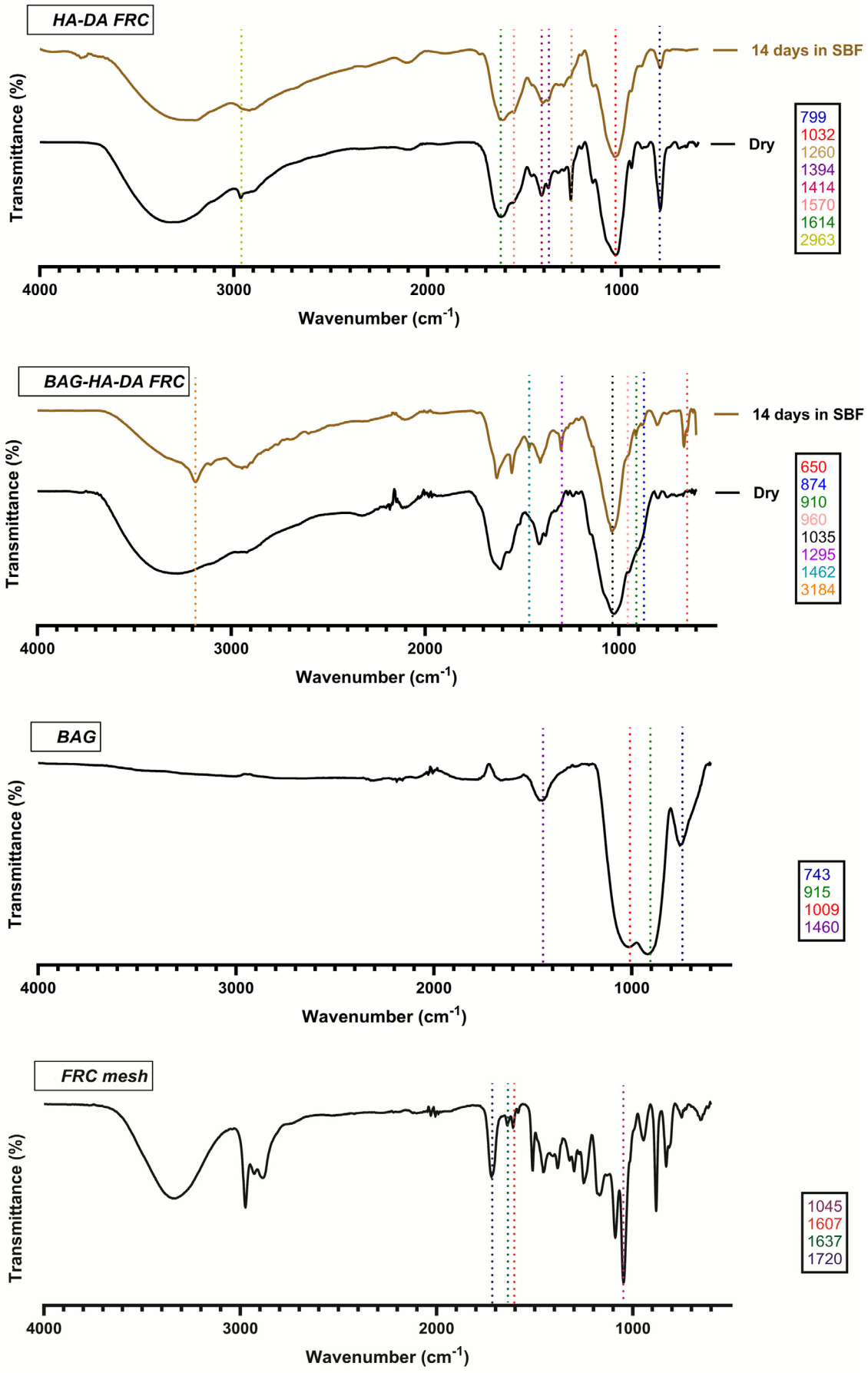


**FIGURE 4** | FTIR spectra of HA-DA FRC (dry and after 14 days in SBF), BAG-HA-DA FRC (dry and after 14 days in SBF), S53P4 BAG (dry), FRC mesh (dry) ($n = 2$).

oxygen (O), chlorine (Cl), and Na as the main elements, consistent with the HA-based hydrogel formulation.

In contrast, BAG-HA-DA FRC scaffolds displayed a rougher hydrogel surface with a higher density of pores compared to the HA-DA FRC (Figure S6C), attributed to the distribution of Si-rich BAG particles throughout the hydrogel. EDX analysis clearly identified Si, traces of Ca and P in addition to C, O, Cl, and Na, thereby confirming the successful incorporation of BAG within the hydrogel matrix. SEM micrographs of the FRC region of the scaffolds displayed the bidirectional orientation of glass fibers made of Si, aluminum (Al), and magnesium (Mg) embedded within a resin matrix primarily composed of C (Figure S6D).

### 3.8 | Degradation and Fluid Uptake in PBS

Degradation profiles along with fluid uptake of the scaffolds are crucial for tissue regeneration, as they both affect their mechanical strength and initial interaction with the surrounding cells. In hydrogel scaffolds, these properties are influenced by various parameters, including the porosity and mesh size of hydrophilic polymeric chains [49]. Enhanced swelling allows a better supply of oxygen, nutrients, and other molecules to the cells [50]. The water uptake capacity of hydrogels is generally governed by internal elastic forces of polymeric chains and osmotic pressure [51].

Plain FRC mesh demonstrated remarkable stability, retaining 99.6% ± 0.6% of its initial weight after 28 days in PBS, confirming its biostable nature (Figure 5A). In contrast, the FRC-hydrogel scaffolds showed controlled degradation, with BAG-HA-DA FRC retaining 85% ± 12% and HA-DA FRC retaining 74% ± 6% of their initial weights. While the degradation results were not in line with stiffness trends since softer hydrogels usually degrade faster, Maquet et al. [52] reported that adding BAG particles to poly-L-lactide increased water absorption while delaying its degradation. Cations released from BAG can reduce the available hydrogen bond donors and acceptors, thereby limiting water-polymer interaction and slowing degradation [38].

Regarding fluid uptake (Figure 5B), FRC mesh showed minimal uptake of only 1% ± 0.1% after 24 h and remained nearly unchanged over the 28-day period. On the other hand, BAG-HA-DA FRC scaffolds displayed the highest fluid uptake after 24 h (44% ± 6%), surpassing the HA-DA FRC scaffolds (21% ± 4%). Notably, both scaffolds displayed a declining trend in uptake thereafter. The higher fluid uptake observed for BAG-HA-DA FRC scaffolds may be related to the lower stiffness of the hydrogel component (Section 3.3), which could facilitate swelling. This observation is consistent with previous reports [38], in which BAG promoted the swelling of gellan gum by increasing water permeability and trapping fluids within the interstices of polymer chains as glass particles dissolved. Conversely, other studies [53] reported that glass incorporation restricted the penetration of the dissolution medium and reduced swelling.

Importantly, no hydrogel detachment from FRC was observed in any samples throughout the 28-day period (Figure S7), suggesting a good wet adhesion of both hydrogels to the FRC.

### 3.9 | pH Changes and Ion Release in PBS

pH changes were evaluated for scaffolds incubated in PBS at different time points over 28 days (Figure 5C). HA-DA FRC scaffolds showed a reduction in pH to 7.22 ± 0.03 on day 1, likely due to degradation of the HA hydrogel component, followed by an increase to 7.37 ± 0.01 on day 3. In contrast, BAG-HA-DA FRC scaffolds exhibited an initial increase in pH, rising from 7.41 at baseline to 7.82 ± 0.13 on day 1, and then decreasing to 7.51 ± 0.03 on day 3, attributed to the release of alkaline cations during BAG dissolution and subsequent ion exchange with $H^+$ ions in the surrounding solution [38]. Subsequently, on day 7, these scaffolds demonstrated a decrease in pH back to baseline levels (7.41 ± 0.01), with no further increase observed until the end of the study, suggesting that most releasable ions from the glass had been depleted.

ICP analysis quantified ion release from the scaffolds during incubation in PBS over a 14-day period (Figure 5D). BAG-HA-DA FRC samples released Ca and Si ions, confirming the reactivity of incorporated BAG particles. Maximum ion release was observed on day 1, after which it declined. Si release ceased after 7 days, while Ca release persisted at lower levels until day 14. This pronounced Ca and Si release, coupled with the observed pH buffering effect, validated the active dissolution and inherent bioactivity of BAG. Although Na and P ions were already present in PBS at high concentrations, both scaffolds exhibited a reduction in P ion levels at the 1st time point. By day 7, BAG-HA-DA scaffolds displayed an increase in P ion concentration.

### 3.10 | Bioactivity of the Scaffolds

The bioactivity of laminate scaffolds was assessed through immersion in SBF for 14 days, with subsequent surface and elemental SEM–EDX analysis. HA-DA FRC scaffolds showed no surface depositions after SBF storage (Figure S8A,B). On the other hand, BAG-HA-DA FRC scaffolds showed distinct nodular structures on the hydrogel surface (Figure S8C). EDX spectra of these deposits revealed Ca and P peaks with Ca/P ratio of 1.69, closely matching the ratio given for hydroxyapatite in literature and implying the bioactivity of the scaffolds [13]. Interestingly, similar Ca–P deposits were also noticed on exposed peripheral FRC areas of the same scaffolds (Figure S8D). This mineralization pattern, observed across both hydrogel and peripheral FRC surfaces, suggests a powerful mechanism for promoting robust bone integration across the entire scaffold.

Further analysis with FTIR corroborated apatite layer formation on BAG-HA-DA FRC scaffolds after 14 days in SBF by tracking distinctive peaks for hydroxyapatite as previously reported [46]. As shown in Figure 4, the composite Si–O–Si/C–O–C band observed in the dry state at 1021 $cm^{-1}$ shifted to nearly 1035 $cm^{-1}$ after incubation, consistent with the formation of phosphate-containing apatite and indicative of BAG dissolution [46]. Peaks near 650 $cm^{-1}$ were observed, corresponding to the $v_4$ bending vibrations (O–P–O) of phosphate groups [54, 55]. The symmetric stretching vibration of phosphate ($\nu 1$) was identified as a shoulder at 962 $cm^{-1}$ accompanied by another shoulder at approximately 910 $cm^{-1}$, which

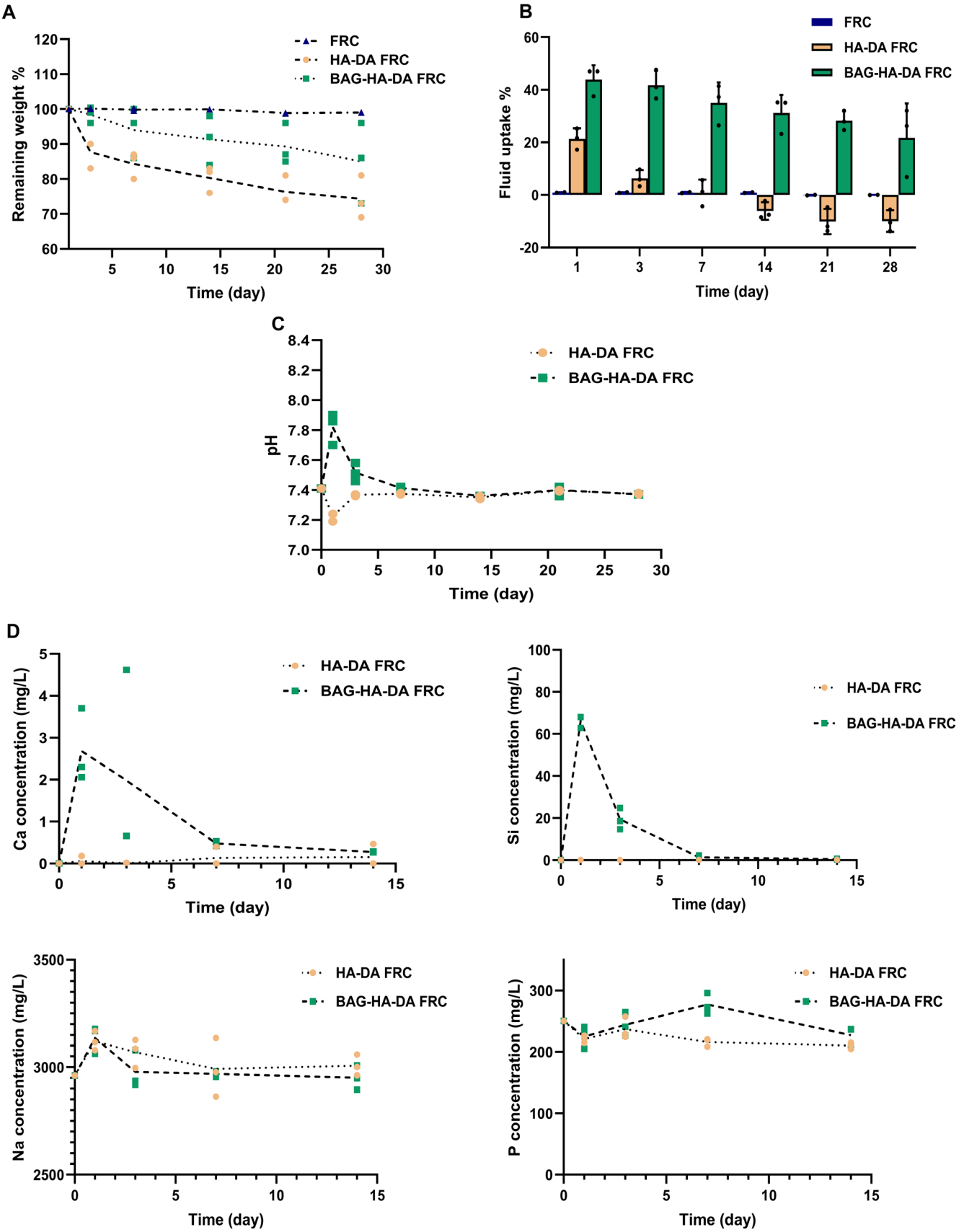


**FIGURE 5** | In vitro degradation profile, pH changes, and ion release kinetics of HA-DA FRC and BAG-HA-DA scaffolds in PBS (pH 7.4) at 37°C ± 0.5°C: (A) Remaining weight (%) ($n = 3$). (B) fluid uptake (%) ($n = 3$). (C) pH changes ($n = 3$). (D) Ion release quantification of Ca, P, Si and Na using ICP-OES over 14 days ($n = 3$). 0-day time point represents the control fresh medium. Zero concentration values indicate measurements below the detection limit of the instrument. The data of (A, B, C, D) are expressed as mean ± SD.

may reflect the presence of poorly crystalline or amorphous calcium phosphate [55]. Additionally, carbonate absorption features appeared by absorption shoulder and peak observed at 874 and 1462 $cm^{-1}$, suggesting B-type carbonate substitution. A change in peak intensity at 1295 $cm^{-1}$ was also observed, further supporting carbonate incorporation [56]. An additional band at 3184 $cm^{-1}$ corresponded to –O-H groups. FTIR spectra collectively indicated the deposition of carbonated apatite layer on BAG-HA-DA FRC scaffolds immersed in SBF, evidencing potential bioactivity. Apatite synthesis can be induced by preferential diffusion-controlled extraction of $Na^+$ and/or $Ca^{2+}$ ions from BAG via exchange with protons from SBF, followed by delayed hydration and dissolution of Si network, creating SiOH surface groups that provide favorable nucleation sites for apatite [15] In HA-DA FRC, only a decrease in peak intensities was observed after SBF incubation.

The degradation of scaffolds in SBF was evaluated over 28 days (Figure 6A). FRC mesh remained stable throughout the whole immersion period. BAG-HA-DA FRC scaffolds displayed higher degradation (67% ± 23% remaining weight) than HA-DA FRC (73% ± 6% remaining weight). This mass change in BAG-HA-DA FRC can be attributed to a dynamic interplay between the hydrolytic breakdown of the hydrogel and the precipitation of Ca–P caused by saturating the solution with ions released by the BAG.

Fluid uptake was highest on day 1, markedly higher in BAG-HA-DA FRC (103% ± 25%) than in HA-DA FRC scaffolds (40% ± 18%) (Figure 6B). By day 7, fluid uptake declined for both scaffolds until the end. FRC was stable across the whole period. None of the scaffolds displayed detachment of the hydrogel from FRC (Figure S7).

The pH of SBF increased to 7.63 ± 0.05 on day 3 and dropped back on day 7 for BAG-HA-DA FRC scaffolds, ending at 7.45 ± 0.2 on day 28 (Figure 6C). In contrast, HA-DA scaffolds showed pH decrease on day 14 and continued till day 28 (7.25 ± 0.1), possibly attributed to the degradation byproducts of HA released into SBF.

Ca ion concentration dropped upon immersing BAG-HA-DA scaffolds in SBF starting from day 1, directly indicating Ca–P layer precipitation (Figure 6D). This was consistent with a study by Astanina et al. [38], where BAG-loaded gellan gum hydrogels caused a decrease in Ca levels of SBF due to hydroxyapatite precipitation. Accordingly, Ca ion concentration measurements supported SEM–EDX and FTIR results, confirming the bioactivity of composite scaffolds.

### 3.11 | Cytocompatibility, Proliferation and Osteogenic Differentiation of Bioprinted BMSCs

Scaffolds biocompatibility was assessed through LIVE/DEAD staining for evaluating the viability of BMSCs printed within the hydrogel component of laminate scaffolds at 1-, 7-, and 14-days post-printing. High cell viability with minimal dead cells was observed in both printed structures at different time points (Figure 7). This robust cell viability confirmed the

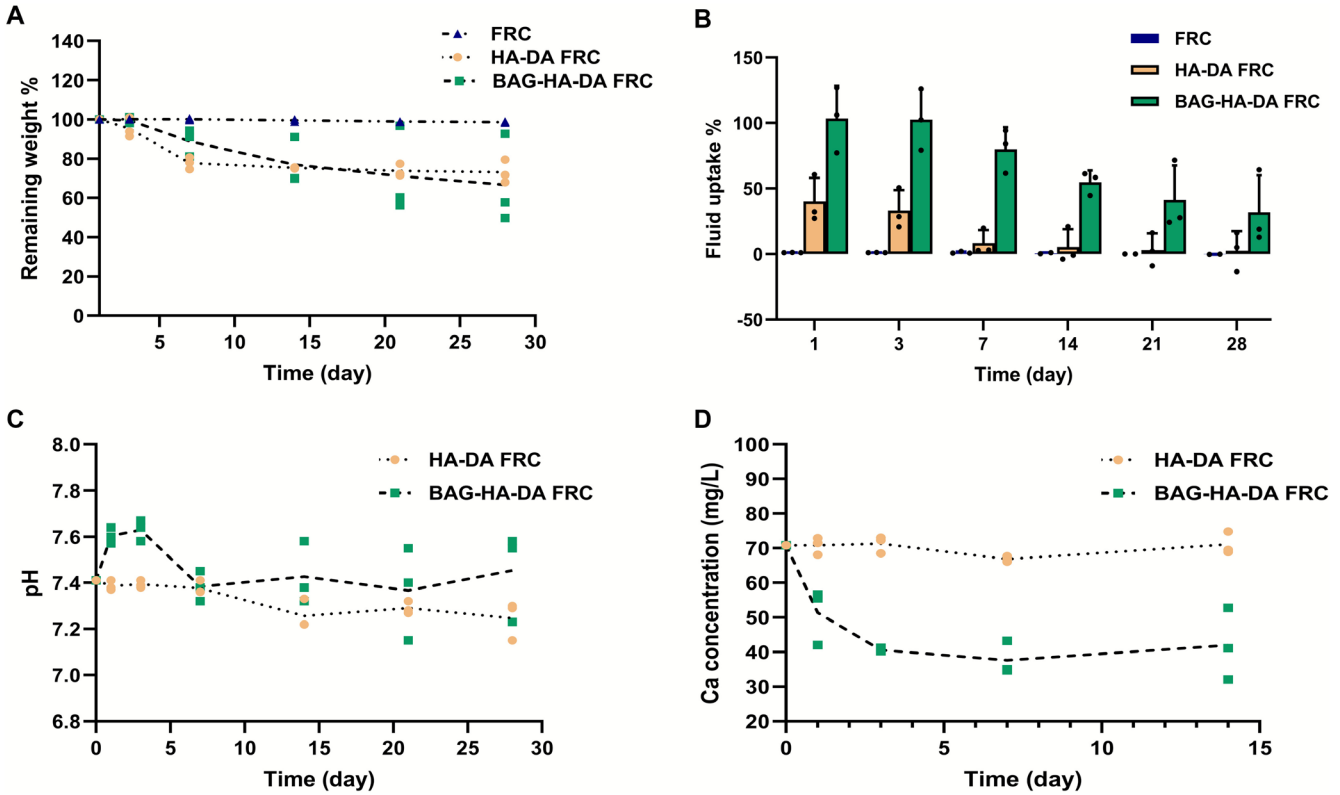


**FIGURE 6** | In vitro degradation profile, pH changes, and Ca ion depletion kinetics of HA-DA FRC and BAG-HA-DA scaffolds in SBF (pH 7.4, non-refreshed) at 37°C ± 0.5°C: (A) Remaining weight % ($n = 3$). (B) Fluid uptake % ($n = 3$). (C) pH changes ($n = 3$). (D) Ca ion concentration ($n = 3$). The data of (A, B, C, D) are expressed as mean ± SD.

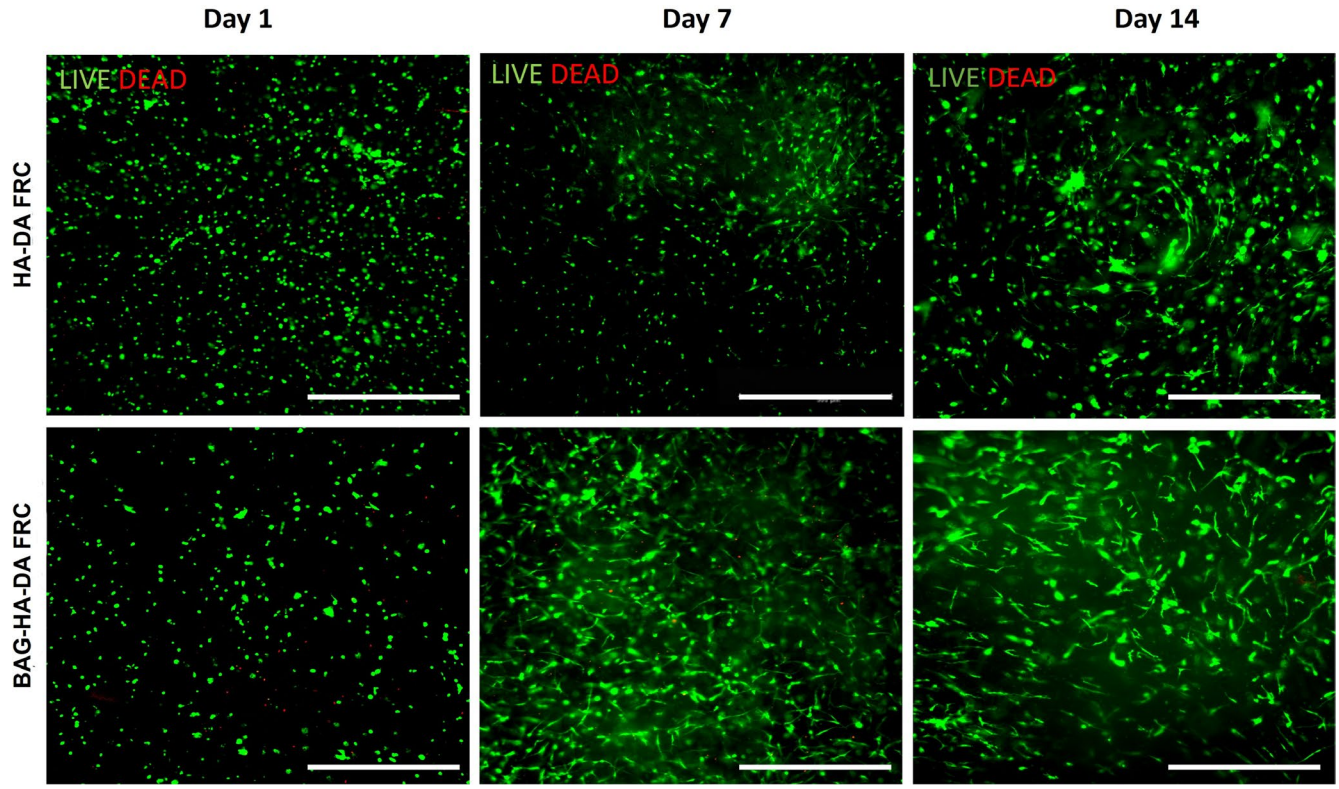


**FIGURE 7** | Live/dead assay of bioprinted BMSCs in HA-DA FRC and BAG-HA-DA FRC scaffolds on days 1, 7 and 14 of culture in osteogenic medium (green = live cells, red = dead cells) ($n = 3$). Scale bar 500 $\mu$m.

cytocompatibility of scaffolds with BMSCs. The high viability on day 1 demonstrated the successful optimization of bioprinting parameters, minimizing shear stress and mechanical cell damage during the extrusion process. The bioink formulation used appeared to provide a protective environment for cells during printing, as the viscoelastic properties of hydrogels can cushion cells during extrusion, thereby reducing mechanical stress while enabling smooth extrusion and maintaining high cell viability [57]. Shear stress is a critical factor affecting cell viability during extrusion-based bioprinting. Although moderate shear stress can enhance the maturation of certain cell types and accelerate stem cell differentiation, [58] excessive shear stress beyond a critical threshold can damage cells and compromise viability [57].

Furthermore, quantitative assessment of the metabolic activity and viability of bioprinted BMSCs with PrestoBlue assay further supported these findings. A significant increase in cellular activity was observed for both scaffold groups from day 1 to day 14 ($p \leq 0.05$) (Figure 8A). On day 7, cells within BAG-HA-DA FRC scaffolds displayed significantly higher metabolic activity than HA-DA FRC ($p = 0.034$). On day 14, cellular metabolic activity was statistically similar ($p = 0.22$) in both scaffolds. The non-significant change on day 14 ($p > 0.05$) aligned with previous studies; stem cell proliferation capacity decreased with osteogenic differentiation [59]. Importantly, adding BAG did not impair cell viability, as previously reported [13]. This likely resulted from decreased hydrogel viscosity and stiffness with BAG addition, increasing water and nutrient uptake, while improving the microenvironment for cell growth.

Cell proliferation, quantified using the CyQUANT assay, increased over time across both groups, indicating that both scaffolds supported cell proliferation, with no significant inter-group differences observed at any time point (Figure 8B). On day 7, higher cell proliferation was observed in BAG-HA-DA FRC scaffolds, suggesting a more rapid initial proliferation phase on this scaffold. From day 7 to day 14, HA-DA FRC showed a sustained but non-significant increase in cell number ($p = 1.00$), whereas the BAG-HA-DA FRC scaffold displayed a non-significant decrease in cell counts ($p = 1.00$).

Alkaline phosphatase, an early osteogenic differentiation marker, was quantified after normalization to cell count (Figure 8C). ALP activity increased significantly from day 7 to day 14 ($p \leq 0.05$) across all scaffolds. Interestingly, HA-DA FRC scaffolds showed significantly higher ALP activity at both time points ($p = 0.05$).

Further assessment of osteogenic differentiation with relative expression of osteogenic marker genes (RUNX2, ALPL, DLX5, and SP7) revealed no significant differences in gene expression across different hydrogel conditions ($p > 0.05$). Both scaffolds supported osteogenic differentiation of BMSCs, confirmed by expression and upregulation of all the analyzed genes from day 7 to day 14 (Figure 8D). However, HA-DA FRC showed higher relative expression levels of all analyzed genes, with a statistically significant increase in ALPL expression between days 7 and 14 ($p = 0.023$). Unexpectedly, despite the confirmed bioactivity and ion release from BAG-HA-DA FRC scaffolds, they did not enhance the early osteogenic commitment, as reflected by ALP activity and osteogenic gene expression of

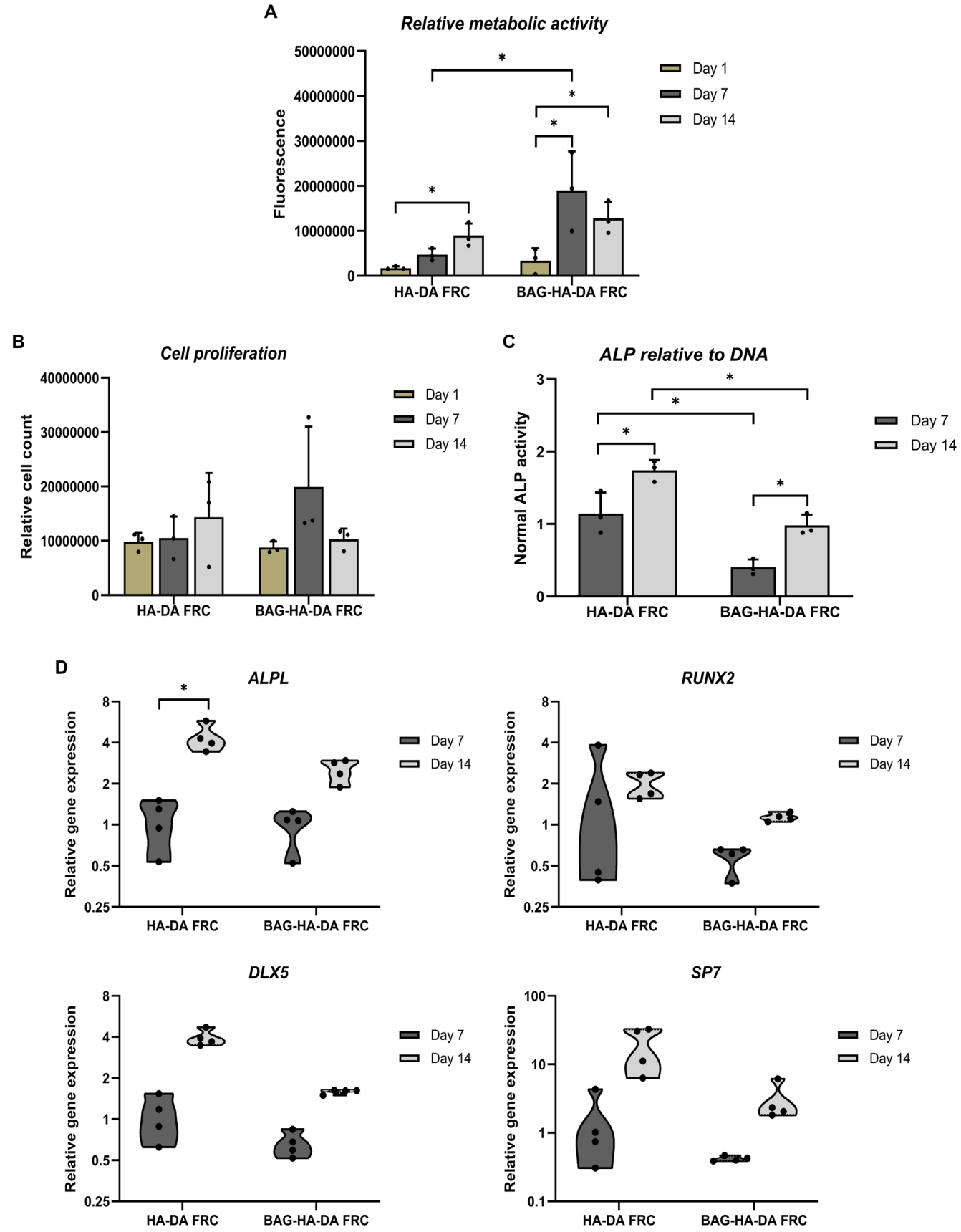


**FIGURE 8** | Legend on next page.

**FIGURE 8** | In vitro assessment of viability and osteogenic differentiation of BMSCs bioprinted within HA-DA FRC and BAG-HA-DA FRC scaffolds: (A) Metabolic activity after 1, 7 and 14 days of culture measured by PrestoBlue assay ($n = 3$). (B) Cell proliferation after 1,7, and 14 days of culture measured by CyQUANT Cell Proliferation Assay (relative DNA content) ($n = 3$). (C) Relative ALP activity normalized to DNA content after 7 and 14 days of culture ($n = 3$). (D) Relative gene expression levels of osteogenic markers RUNX2, ALPL, DLX5, and SP7 after 7 and 14 days of culture quantified by qRT-PCR ($n = 4$). Gene expression levels are shown relative to HA-DA FRC scaffold after 7 days of culture; GAPDH was used as a reference gene to normalize the gene expression levels. * $p \leq 0.05$. The data of (A, B, C) are expressed as the means ± SD.

BMSCs. This contrasts with previous reports [13, 60] where BAG promoted osteogenic differentiation of mesenchymal stem cells in stiffer or ionically crosslinked matrices, through the ionic dissolution products [30, 59, 61] and activation of signaling pathways crucial for directing stem cell fate toward osteogenesis [62].

Despite the low stiffness of the investigated hydrogel (< 250 Pa), our findings were in line with a previous study by Jha et al. [63] conducted on soft hydrogels (stiffness 102–970 Pa), where stiffer hydrogel matrices supported early osteogenic differentiation of BMSCs, mean while softer ones favored cell proliferation. The lack of significant early osteogenic differentiation at 1% (w/v) BAG used in this study may be attributed to insufficient biochemical cues in combination with the markedly low hydrogel stiffness. A more comprehensive analysis at late time points is recommended to determine the effect of BAG on the late osteogenic differentiation of the cells.

The current study suggests important design principles for incorporating BAG into chemically pH-sensitive HA hydrogel systems, within the constraints of the tested BAG concentration and time frame. Unlike chemically compatible ionically-crosslinked hydrogels, where BAG incorporation enhanced their mechanical properties [13, 38], the hydrazone-crosslinked HA-DA system showed reduced stiffness due to pH-induced crosslinking impairment. This highlights the need for matching bioactive filler chemistry with the crosslinking mechanism of the polymer network. Optimization strategies such as modulation of BAG loading or use of less alkalizing types of BAG can be considered for future investigation.

Finally, while 10 mg/mL (1% w/v) of BAG provided significant insights into the chemical interplay with the hydrazone-crosslinked matrix, this study was limited by investigating a single BAG concentration, limiting the assessment of dose-dependent effects on hydrogel properties and osteogenic differentiation. Furthermore, osteogenic evaluation was limited to early-stage markers (ALP and early gene expression). Late-stage markers such as matrix mineralization and extended cell culture periods would provide a more comprehensive understanding.

## 4 | Conclusions

In this study, a laminate scaffold was developed by integrating a biodegradable 3D-printed HA-based bioink with a biostable FRC. Two scaffold variants were investigated: HA-DA FRC and a modified version incorporating BAG particles, BAG-HA-DA FRC. BAG addition significantly altered the hydrogel characteristics by reducing viscosity and stiffness while increasing fluid uptake and swelling. These changes were attributed to the alkaline pH shift induced by BAG, which interfered with the pH-sensitive hydrazone crosslinking reaction specific to the investigated HA-DA system. Despite these effects on hydrogel mechanics, controlled ion release from BAG promoted mineralization and apatite formation.

Both scaffold variants exhibited excellent cytocompatibility, supporting high viability and proliferation of encapsulated BMSCs. Moreover, early osteogenic differentiation was supported, as indicated by ALP activity as well as the expression and upregulation of osteogenic marker genes. However, within the investigated stiffness range and BAG concentration, the BAG-HA-DA FRC system did not result in enhanced early osteogenic differentiation compared to the BAG-free scaffold. These findings emphasize the importance of understanding hydrogel chemistry, crosslinking mechanisms, and polymer matrix-inorganic fillers interaction for a successful composite design.

In conclusion, the developed laminate FRC-hydrogel scaffolds represent a promising platform for bone regeneration application. The design offers a framework for further advancement in employing stem cell therapy and bioink-based treatments for repairing bone defects through the fabrication of patient-specific implantable devices. In addition, vascular cells can be introduced into the system and investigated for the generation of scaffolds with vascularization as a future substitute for bone flaps. While the demonstrated biocompatibility supports the potential of this system for future translational applications, further long-term and in vivo studies are required to validate its suitability for clinical use.

### Author Contributions

**Mona Gibreel**, **Roope Ohlsbom**, and **Leila Perea-Lowery:** conceptualization, investigation, methodology, visualization, writing – original draft, writing – review and editing. **Lippo Lassila:** conceptualization, investigation, methodology, writing – review and editing. **Paula Puistola** and **Karoliina Hopia:** conceptualization, investigation, methodology, visualization, writing – review and editing. **Susanna Miettinen:** conceptualization, funding acquisition, resources, methodology, project administration, resources, supervision, writing – review and editing. **Anni Mörö:** conceptualization, funding acquisition, methodology, project administration, resources, supervision, writing – review and editing. **Pekka K. Vallittu:** conceptualization, funding acquisition, project administration, methodology, resources, supervision, validation, writing – review and editing.

### Acknowledgments

The authors would like to acknowledge Materials Research Infrastructure (MARI) at the Department of Physics and Astronomy, University of Turku for access and support with the SEM facilities and Timo Peltola, StickTech (member of the GC group) for technical

assistance with SEM. Figure 1 was created in BioRender. https://BioRender.com/e94h138. During the preparation of this work, the authors used Microsoft Copilot, Gemini Ai, and BLACKBOX Ai in order to improve readability and language. After using this tool, the content was reviewed and edited by the authors as needed, who take full responsibility for the content of the publication.

### Funding

This work was supported by grants from Suomen Lääketieteen Säätiö (Grant 5772 (MG)); Research Council of Finland (Project CEBON 357142 (PV) and Project CoEBoC 336666 (SM)); Business Finland (Project IMD1 11/31/2023 (PV) and Research to Business Project 6763/31/2021 (AM)). This study was financially supported by the State Funding for University-Level Health Research, Tampere University Hospital, Wellbeing Services County of Pirkanmaa, Tampere, Finland.

### Conflicts of Interest

Anni Mörö is an inventor of a pending patent application related to the bioink innovation reported in this study. Based on the Act on the Right in Inventions in Finland, all authors employed by Tampere University have given all rights to the University and thus have declared no competing interests. The other authors declare no conflicts of interest.

### Data Availability Statement

The data that support the findings of this study are available on request from the corresponding author. The data are not publicly available due to privacy or ethical restrictions.

### References

1. N. Reznikov, R. Shahar, and S. Weiner, "Bone Hierarchical Structure in Three Dimensions," *Acta Biomaterialia* 10 (2014): 3815–3826.

2. A. M. Weatherholt, R. K. Fuchs, and S. J. Warden, "Specialized Connective Tissue: Bone, the Structural Framework of the Upper Extremity," *Journal of Hand Therapy* 25 (2012): 123–132.

3. R. S. Taichman, "Blood and Bone: Two Tissues Whose Fates Are Intertwined to Create the Hematopoietic Stem-Cell Niche," *Blood* 105 (2005): 2631–2639.

4. S.-C. Lee, J.-F. Chen, C.-T. Wu, and S.-T. Lee, "In Situ Local Autograft for Instrumented Lower Lumbar or Lumbosacral Posterolateral Fusion," *Journal of Clinical Neuroscience* 16 (2009): 37–43.

5. G. M. Calori, E. Mazza, M. Colombo, and C. Ripamonti, "The Use of Bone-Graft Substitutes in Large Bone Defects: Any Specific Needs?," *Injury* 42 (2011): S56–S63.

6. W. Zhao, X. Jin, Y. Cong, Y. Liu, and J. Fu, "Degradable Natural Polymer Hydrogels for Articular Cartilage Tissue Engineering," *Journal of Chemical Technology and Biotechnology* 88 (2013): 327–339.

7. R. Silva, B. Fabry, and A. R. Boccaccini, "Fibrous Protein-Based Hydrogels for Cell Encapsulation," *Biomaterials* 35 (2014): 6727–6738.

8. A. Mörö, S. Samanta, L. Honkamäki, et al., "Hyaluronic Acid Based Next Generation Bioink for 3D Bioprinting of Human Stem Cell Derived Corneal Stromal Model With Innervation," *Biofabrication* 15 (2022): 035010.

9. Y.-W. Ding, X.-W. Zhang, C.-H. Mi, X.-Y. Qi, J. Zhou, and D.-X. Wei, "Recent Advances in Hyaluronic Acid-Based Hydrogels for 3D Bioprinting in Tissue Engineering Applications," *Smart Materials in Medicine* 4 (2023): 59–68.

10. M. P. Sekar, S. Suresh, A. Zennifer, S. Sethuraman, and D. Sundaramurthi, "Hyaluronic Acid as Bioink and Hydrogel Scaffolds for Tissue Engineering Applications," *ACS Biomaterials Science & Engineering* 9 (2023): 3134–3159.

11. K. Vuornos, M. Ojansivu, J. T. Koivisto, et al., "Bioactive Glass Ions Induce Efficient Osteogenic Differentiation of Human Adipose Stem Cells Encapsulated in Gellan Gum and Collagen Type I Hydrogels," *Materials Science & Engineering, C: Materials for Biological Applications* 99 (2019): 905–918.

12. P. Puistola, S. Miettinen, H. Skottman, and A. Mörö, "Novel Strategy for Multi-Material 3D Bioprinting of Human Stem Cell Based Corneal Stroma With Heterogenous Design," *Materials Today Bio* 24 (2024): 100924.

13. M. Ojansivu, A. Rashad, A. Ahlinder, et al., "Wood-Based Nanocellulose and Bioactive Glass Modified Gelatin-Alginate Bioinks for 3D Bioprinting of Bone Cells," *Biofabrication* 11 (2019): 035010.

14. T. Gong, J. Xie, J. Liao, T. Zhang, S. Lin, and Y. Lin, "Nanomaterials and Bone Regeneration," *Bone Research* 3 (2015): 1–7.

15. J. R. Jones, "Review of Bioactive Glass: From Hench to Hybrids," *Acta Biomaterialia* 9 (2013): 4457–4486.

16. S. Nazari, M. Naeimi, M. Rafienia, and M. Monajjemi, "Fabrication and Characterization of 3D Nanostructured Polycaprolactone-Gelatin/Nanohydroxyapatite-Nanoclay Scaffolds for Bone Tissue Regeneration," *Journal of Polymers and the Environment* 32 (2024): 94–110.

17. I. Hernandez, A. Kumar, and B. Joddar, "A Bioactive Hydrogel and 3D Printed Polycaprolactone System for Bone Tissue Engineering," *Gels* 3 (2017): 26.

18. N. Dubey, J. A. Ferreira, A. Daghrery, et al., "Highly Tunable Bioactive Fiber-Reinforced Hydrogel for Guided Bone Regeneration," *Acta Biomaterialia* 113 (2020): 164–176.

19. H. Yilmaz, T. Bedir, S. Gursoy, et al., "Development of Bilayer Tissue-Engineered Scaffolds: Combination of 3D Printing and Electrospinning Methodologies," *Biomedical Materials* 19 (2024): 045001.

20. A. M. Ballo, I. Cekic-Nagas, G. Ergun, et al., "Osseointegration of Fiber-Reinforced Composite Implants: Histological and Ultrastructural Observations," *Dental Materials* 30 (2014): e384–e395.

21. R. H. Mattila, P. Laurila, J. Rekola, et al., "Bone Attachment to Glass-Fibre-Reinforced Composite Implant With Porous Surface," *Acta Biomaterialia* 5 (2009): 1639–1646.

22. A. Väisänen, N. Hoikkala, V. Härkönen, N. Moritz, and P. K. Vallittu, "Biomechanical Considerations of Semi-Anatomic Glass Fiber-Reinforced (GFRC) Composite Implant for Mandibular Segmental Defects: A Technical Note," *Journal of the Mechanical Behavior of Biomedical Materials* 156 (2024): 106604.

23. K. M. J. Aitasalo, J. M. Piitulainen, J. Rekola, and P. K. Vallittu, "Craniofacial Bone Reconstruction With Bioactive Fiber-Reinforced Composite Implant," *Head & Neck* 36 (2014): 722–728.

24. P. K. Vallittu, "Fiber-Reinforced Composites for Implant Applications," *Current Oral Health Reports* 5 (2018): 194–201.

25. S. M.-R. Tuusa, M. J. Peltola, T. Tirri, L. V. J. Lassila, and P. K. Vallittu, "Frontal Bone Defect Repair With Experimental Glass-Fiber-Reinforced Composite With Bioactive Glass Granule Coating," *Journal of Biomedical Materials Research Part B: Applied Biomaterials* 82B (2007): 149–155.

26. A. M. Ballo, L. V. Lassila, P. K. Vallittu, and T. O. Närhi, "Load Bearing Capacity of Bone Anchored Fiber-Reinforced Composite Device," *Journal of Materials Science: Materials in Medicine* 18 (2007): 2025–2031.

27. A. Shinya, A. M. Ballo, L. V. J. Lassila, A. Shinya, T. O. Närhi, and P. K. Vallittu, "Stress and Strain Analysis of the Bone-Implant Interface: A Comparison of Fiber-Reinforced Composite and Titanium Implants Utilizing 3-Dimensional Finite Element Study," *Journal of Oral Implantology* 37 (2011): 133–140.

28. A. M. Ballo, A. K. Kokkari, V. V. Meretoja, L. L. Lassila, P. K. Vallittu, and T. O. Narhi, "Osteoblast Proliferation and Maturation on

Bioactive Fiber-Reinforced Composite Surface," *Journal of Materials Science: Materials in Medicine* 19 (2008): 3169–3177.

29. A. M. Ballo, E. A. Akca, T. Ozen, L. Lassila, P. K. Vallittu, and T. O. Närhi, "Bone Tissue Responses to Glass Fiber-Reinforced Composite Implants—A Histomorphometric Study," *Clinical Oral Implants Research* 20 (2009): 608–615.

30. M. Bosetti and M. Cannas, "The Effect of Bioactive Glasses on Bone Marrow Stromal Cells Differentiation," *Biomaterials* 26 (2005): 3873–3879.

31. A. A. Abdulmajeed, A. K. Kokkari, J. Käpylä, et al., "In Vitro Blood and Fibroblast Responses to BisGMA–TEGDMA/Bioactive Glass Composite Implants," *Journal of Materials Science: Materials in Medicine* 25 (2014): 151–162.

32. M. Väkiparta, M. Puska, and P. K. Vallittu, "Residual Monomers and Degree of Conversion of Partially Bioresorbable Fiber-Reinforced Composite," *Acta Biomaterialia* 2 (2006): 29–37.

33. D. Y. Kwok and A. W. Neumann, "Contact Angle Measurement and Contact Angle Interpretation," *Advances in Colloid and Interface Science* 81 (1999): 167–249.

34. T. Kokubo, "Bioactive Glass Ceramics: Properties and Applications," *Biomaterials* 12 (1991): 155–163.

35. A. Gebraad, R. Kornilov, S. Kaur, et al., "Monocyte-Derived Extracellular Vesicles Stimulate Cytokine Secretion and Gene Expression of Matrix Metalloproteinases by Mesenchymal Stem/Stromal Cells," *FEBS Journal* 285 (2018): 2337–2359.

36. K. J. Livak and T. D. Schmittgen, "Analysis of Relative Gene Expression Data Using Real-Time Quantitative PCR and the 2(-Delta Delta C(T)) Method," *Methods* 25 (2001): 402–408.

37. A. Ylä-Soininmäki, N. Moritz, L. V. J. Lassila, M. Peltola, H. T. Aro, and P. K. Vallittu, "Characterization of Porous Glass Fiber-Reinforced Composite (FRC) Implant Structures: Porosity and Mechanical Properties," *Journal of Materials Science: Materials in Medicine* 24 (2013): 2683–2693.

38. A. Astanina, J. T. Koivisto, M. Hannula, T. Salminen, M. Kellomäki, and J. Massera, "Chemical Interactions in Composites of Gellan Gum and Bioactive Glass: Self-Crosslinking and in Vitro Dissolution," *Frontiers in Chemistry* 11 (2023): 1133374.

39. L. Koivusalo, J. Karvinen, E. Sorsa, et al., "Hydrazone Crosslinked Hyaluronan-Based Hydrogels for Therapeutic Delivery of Adipose Stem Cells to Treat Corneal Defects," *Materials Science & Engineering, C: Materials for Biological Applications* 85 (2018): 68–78.

40. D. D. McKinnon, D. W. Domaille, J. N. Cha, and K. S. Anseth, "Bis-Aliphatic Hydrazone-Linked Hydrogels Form Most Rapidly at Physiological pH: Identifying the Origin of Hydrogel Properties With Small Molecule Kinetic Studies," *Chemistry of Materials* 26 (2014): 2382–2387.

41. S. Pramanik, F. Ataollahi, B. Pingguan-Murphy, A. A. Oshkour, and N. A. A. Osman, "In Vitro Study of Surface Modified Poly(Ethylene Glycol)-Impregnated Sintered Bovine Bone Scaffolds on Human Fibroblast Cells," *Scientific Reports* 5 (2015): 9806.

42. M. Strobel and C. S. Lyons, "An Essay on Contact Angle Measurements," *Plasma Processes and Polymers* 8 (2011): 8–13.

43. D. Hauser, D. Septiadi, J. Turner, A. Petri-Fink, and B. Rothen-Rutishauser, "From Bioinspired Glue to Medicine: Polydopamine as a Biomedical Material," *Materials* 13 (2020): 1730.

44. N. Pandey, L. F. Soto-Garcia, J. Liao, P. Zimmern, K. T. Nguyen, and Y. Hong, "Mussel-Inspired Bioadhesives in Healthcare: Design Parameters, Current Trends, and Future Perspectives," *Biomaterials Science* 8 (2020): 1240.

45. P. A. Forero-Sossa, J. D. Salazar-Martinez, V. J. Barajas-Aguilar, et al., "Effect of S53P4 Bioactive Glass Content on Structural and in-Vitro Behavior of Hydroxyapatite/Bioactive Glass Mixtures Prepared by Mechanical Milling," *Ceramics International* 49 (2023): 4322–4330.

46. H. Faqhiri, M. Hannula, M. Kellomäki, M. T. Calejo, and J. Massera, "Effect of Melt-Derived Bioactive Glass Particles on the Properties of Chitosan Scaffolds," *Journal of Functional Biomaterials* 10 (2019): 38.

47. Z. Okulus, T. Buchwald, M. Szybowicz, and A. Voelkel, "Study of a New Resin-Based Composites Containing Hydroxyapatite Filler Using Raman and Infrared Spectroscopy," *Materials Chemistry and Physics* 145 (2014): 304–312.

48. A. H. S. Delgado and A. M. Young, "Methacrylate Peak Determination and Selection Recommendations Using ATR-FTIR to Investigate Polymerisation of Dental Methacrylate Mixtures," *PLoS One* 16 (2021): e0252999.

49. A. Kumar and S. S. Han, "Enhanced Mechanical, Biomineralization, and Cellular Response of Nanocomposite Hydrogels by Bioactive Glass and Halloysite Nanotubes for Bone Tissue Regeneration," *Materials Science and Engineering C* 128 (2021): 112236.

50. H. Park, X. Guo, J. S. Temenoff, et al., "Effect of Swelling Ratio of Injectable Hydrogel Composites on Chondrogenic Differentiation of Encapsulated Rabbit Marrow Mesenchymal Stem Cells in Vitro," *Biomacromolecules* 10 (2009): 541–546.

51. T. Cano, H. Na, J. Sun, and H. Kim, "Swelling Kinetics of Constrained Hydrogel Spheres," *Soft Matter* 19 (2023): 8820–8831.

52. V. Maquet, A. R. Boccaccini, L. Pravata, I. Notingher, and R. Jérôme, "Porous Poly(α-Hydroxyacid)/bioglass Composite Scaffolds for Bone Tissue Engineering. I: Preparation and in Vitro Characterisation," *Biomaterials* 25 (2004): 4185–4194.

53. J. Zheng, F. Zhao, W. Zhang, et al., "Sequentially-Crosslinked Biomimetic Bioactive Glass/Gelatin Methacryloyl Composites Hydrogels for Bone Regeneration," *Materials Science & Engineering, C: Materials for Biological Applications* 89 (2018): 119–127.

54. M. S. Hossain and S. Ahmed, "FTIR Spectrum Analysis to Predict the Crystalline and Amorphous Phases of Hydroxyapatite: A Comparison of Vibrational Motion to Reflection," *RSC Advances* 13 (2023): 14625–14630.

55. C. W. Chen, C. S. Oakes, K. Byrappa, et al., "Synthesis, Characterization, and Dispersion Properties of Hydroxyapatite Prepared by Mechanochemical–Hydrothermal Methods," *Journal of Materials Chemistry* 14 (2004): 2425–2432.

56. A. Malekpour and X. Chen, "Printability and Cell Viability in Extrusion-Based Bioprinting From Experimental, Computational, and Machine Learning Views," *Journal of Functional Biomaterials* 13 (2022): 40.

57. C. M. F. Potter, K. H. Lao, L. Zeng, and Q. Xu, "Role of Biomechanical Forces in Stem Cell Vascular Lineage Differentiation," *Arteriosclerosis, Thrombosis, and Vascular Biology* 34 (2014): 2184–2190.

58. M. Ojansivu, S. Vanhatupa, L. Björkvik, et al., "Bioactive Glass Ions as Strong Enhancers of Osteogenic Differentiation in Human Adipose Stem Cells," *Acta Biomaterialia* 21 (2015): 190–203.

59. A. Gantar, L. P. da Silva, J. M. Oliveira, et al., "Nanoparticulate Bioactive-Glass-Reinforced Gellan-Gum Hydrogels for Bone-Tissue Engineering," *Materials Science and Engineering C* 43 (2014): 27–36.

60. Y. Ai, F. Dai, W. Li, et al., "Photo-Crosslinked Bioactive BG/BMSCs@GelMA Hydrogels for Bone-Defect Repairs," *Materials Today Bio* 23 (2023): 100882.

61. M. Waselau, M. Patrikoski, M. Juntunen, et al., "Effects of Bioactive Glass S53P4 or Beta-Tricalcium Phosphate and Bone Morphogenetic Protein-2 and Bone Morphogenetic Protein-7 on Osteogenic Differentiation of Human Adipose Stem Cells," *Journal of Tissue Engineering* 3 (2012): 2041731412467789.

62. Y. Guo, Y. Xue, W. Niu, et al., "Monodispersed Bioactive Glass Nanoparticles Enhance the Osteogenic Differentiation of Adipose-Derived Stem Cells Through Activating TGF-Beta/Smad3

Signaling Pathway," *Particle & Particle Systems Characterization* 35 (2018): 1800087.

63. A. K. Jha, W. M. Jackson, and K. E. Healy, "Controlling Osteogenic Stem Cell Differentiation via Soft Bioinspired Hydrogels," *PLoS One* 6 (2014): e98640.

**Supporting Information**

Additional supporting information can be found online in the Supporting Information section. **Data S1.** Supporting Information.